



Chinese Pharmaceutical Association
Institute of Materia Medica, Chinese Academy of Medical Sciences

Acta Pharmaceutica Sinica B

www.elsevier.com/locate/apsb
www.sciencedirect.com



ORIGINAL ARTICLE

Multidimensional autophagy nano-regulator boosts Alzheimer's disease treatment by improving both extra/intraneuronal homeostasis



Yixian Li[†], Peng Yang[†], Ran Meng[†], Shuting Xu, Lingling Zhou, Kang Qian, Pengzhen Wang, Yunlong Cheng, Dongyu Sheng, Minjun Xu, Tianying Wang, Jing Wu, Jinxu Cao, Qizhi Zhang*

Key Laboratory of Smart Drug Delivery, Ministry of Education, School of Pharmacy, Fudan University, Shanghai 201203, China

Received 11 July 2023; received in revised form 27 September 2023; accepted 28 September 2023

KEY WORDS

Autophagy-lysosome pathway;
Alzheimer's disease;
Proteostasis;
Neuroinflammation;
Multi-target therapy;
Rapamycin;
Gypenoside XVII;
Cascade dual-targeting

Abstract Intraneuronal dysproteostasis and extraneuronal microenvironmental abnormalities in Alzheimer's disease (AD) collectively culminate in neuronal deterioration. In the context of AD, autophagy dysfunction, a multi-link obstacle involving autophagy downregulation and lysosome defects in neurons/microglia is highly implicated in intra/extraneuronal pathological processes. Therefore, multidimensional autophagy regulation strategies co-manipulating “autophagy induction” and “lysosome degradation” in dual targets (neuron and microglia) are more reliable for AD treatment. Accordingly, we designed an RP-1 peptide-modified reactive oxygen species (ROS)-responsive micelles (RT-NM) loading rapamycin or gypenoside XVII. Guided by RP-1 peptide, the ligand of receptor for advanced glycation end products (RAGE), RT-NM efficiently targeted neurons and microglia in AD-affected region. This nano-combination therapy activated the whole autophagy-lysosome pathway by autophagy induction (rapamycin) and lysosome improvement (gypenoside XVII), thus enhancing autophagic degradation of neurotoxic aggregates and inflammasomes, and promoting $A\beta$ phagocytosis. Resultantly, it decreased aberrant protein burden, alleviated neuroinflammation, and eventually ameliorated memory defects in $3 \times$ Tg-AD transgenic mice. Our research developed a multidimensional autophagy nano-regulator to boost the efficacy of autophagy-centered AD therapy.

*Corresponding author.

E-mail address: qzhang@fudan.edu.cn (Qizhi Zhang).

[†]These authors made equal contributions to this work.

Peer review under the responsibility of Chinese Pharmaceutical Association and Institute of Materia Medica, Chinese Academy of Medical Sciences.

<https://doi.org/10.1016/j.apsb.2023.10.009>

2211-3835 © 2024 The Authors. Published by Elsevier B.V. on behalf of Chinese Pharmaceutical Association and Institute of Materia Medica, Chinese Academy of Medical Sciences. This is an open access article under the CC BY-NC-ND license (<http://creativecommons.org/licenses/by-nc-nd/4.0/>).

© 2024 The Authors. Published by Elsevier B.V. on behalf of Chinese Pharmaceutical Association and Institute of Materia Medica, Chinese Academy of Medical Sciences. This is an open access article under the CC BY-NC-ND license (<http://creativecommons.org/licenses/by-nc-nd/4.0/>).

1. Introduction

Autophagy, an important self-digestive mechanism for pathogenic proteins clearance¹, is profoundly intertwined with Alzheimer's disease (AD) pathogenesis which is characterized by the deposition of intracellular and extracellular toxic aggregates, including extracellular amyloid plaque deposits composed of agglomerated amyloid β -protein ($A\beta$), as well as intracellular neurofibrillary tangles (NFTs) consisting of hyperphosphorylated tau protein². Numerous autophagy-targeted therapies have been investigated to combat these two toxic aggregates-induced AD pathologies, especially in neurons - the central diseased cell population suffering severe dysproteostasis^{3,4}. However, neuronal autophagy is limited to decomposing intraneuronal aggregates, doing little to degrade extraneuronal ones. With the deepening of related research, the uncovered ability of microglial autophagy in normalizing extraneuronal microenvironment extends the significance of autophagy regulation beyond the clearance of intracellular toxic substances. Concretely, microglial autophagy has been verified to facilitate the removal of extracellular $A\beta$ deposits on the grounds of its functional cross-talk with phagocytosis^{5,6}. In addition, microglial autophagy also participates in neuroinflammation regulation *via* negative modulation of nucleotide-binding domain and leucine-rich repeat protein 3 (NLRP3) inflammasome which is a key multimeric protein complex in the AD-related inflammatory pathway^{7,8}. In view of the above, it is deduced that co-regulating neuronal and microglial autophagy would concurrently maintain neuronal proteostasis and improve pathological microenvironment, thereby achieving dual neuroprotection to enhance therapeutic efficacy.

It is worth noting that autophagy is a dynamic multi-link process in which nascent autophagosomes are constantly emerging, maturing, degrading, and recycling⁹, providing multifarious candidate links for regulation. The rational selection of interference links is a crucial part of strategizing autophagy regulation. In AD, besides the inhibited autophagy activity, the imbalance of autophagosome formation and degradation which is attributed to lysosomal impairment is also a prominent feature of autophagy dysfunction¹⁰. This accounts in part for the failure of sole autophagy-activating strategies, since these strategies may further burden pathological lysosomes and aggravate autophagosome accumulation⁴. Reasonably, the combination of autophagy activation and lysosome restoration, which can enhance autophagy flux (the entire process of autophagosome formation and autophagic degradation), holds great promise in fully realizing the therapeutic potential of autophagy regulation for AD.

Rapamycin (Rapa), a specific inhibitor of the mammalian target of rapamycin complex 1 (mTORC1), is recognized as an efficient and safe autophagy inducer that can promote autophagosome generation and activate autophagy^{11,12}. Gypenoside XVII (GP-17) possessing a promotive effect on the nuclear translocation of transcription factor EB (TFEB), a main transcription factor regulating the expression of lysosome-related genes, is documented to enhance lysosome biogenesis and improve lysosomal function¹³. Accordingly, the combined administration of Rapa and GP-17 is

anticipated to co-regulate autophagosome biogenesis and lysosomal degradation. To emphasize, considering the double-edged nature of autophagy^{14,15}, it is a necessity to heighten the lesion site- and target cell-specificity of drug delivery to guarantee therapeutic outcomes and avoid side effects of systemic autophagy induction. In this regard, there exist at least the following obstacles: (1) Rapa and GP-17 have poor solubility and low blood-brain barrier (BBB) permeability^{16,17}. (2) After BBB penetration, drugs should be enriched in both microglia and neurons. (3) Most nano-carriers are degraded through the endo-lysosome pathway and further release drugs^{18,19}. Compromised lysosomes in AD neurons and microglia may hamper their intracellular drug release. To overcome these problems, the delivery system should be elaborately designed. Reactive oxygen species (ROS) has been considered as an attracting utilizable pathologic feature for intelligent drug delivery system design in AD^{20,21}. Our previous work constructed a ROS-responsive micelle composed of poly (ethylene glycol)-thioketal-polycaprolactone (PEG-TK-PCL) polymer to load hydrophobic drugs²². This micelle can quickly disrupt and release drugs in the pathological environment of AD with high ROS and its ROS-assisted degradation also reduces the burden of pathological lysosomes. Moreover, it has been revealed that the expression of the receptor for advanced glycation end products (RAGE) is upregulated on BBB, neurons, and microglia in the pathological region of AD patients^{23–25}. We also found the significantly increased RAGE level in $3 \times$ Tg-AD mice brains to wild-type counterparts (Supporting Information Fig. S1). RP-1 peptide (sequence: CAPDTKTQ), a non-toxic phage-displayed peptide, has a high affinity with RAGE²⁶, thereby this peptide is a suitable targeting ligand to mediate micellar BBB penetration and subsequent localization to neuron and microglia in AD-affected region. Based on the aforementioned concepts, RP-1-modified ROS-responsive micelle systems that loaded with Rapa (RT-NM/Rapa) or GP-17 (RT-NM/GP-17) were fabricated in this study (Fig. 1).

Thanks to the multi-targetability and ROS-responsiveness of the drug-loaded micelle system, the regulative action of Rapa and GP-17 combination on autophagy was greatly exerted. Our results confirmed the superior therapeutic effects of the combined micelle [RT-NM/(Rapa + GP-17)] treatment on $3 \times$ Tg-AD transgenic mice. RT-NM/(Rapa + GP-17) efficiently activated the entire autophagy-lysosome pathway, consequently reducing pathological protein accumulation, mitigating neuroinflammation, and improving cognitive performance. This study explored a multidimensional, systemic, and comprehensive autophagy-modulating therapeutic strategy whose design is more in line with the AD pathological states, thereby maximizing the therapeutic benefits of autophagy regulation for AD treatment.

2. Materials and methods

2.1. Materials

Rapamycin (Rapa), coumarin-6 (Cou-6), and okadaic acid (OA) were purchased from Sigma-Aldrich Inc. (St. Louis, MO, USA).

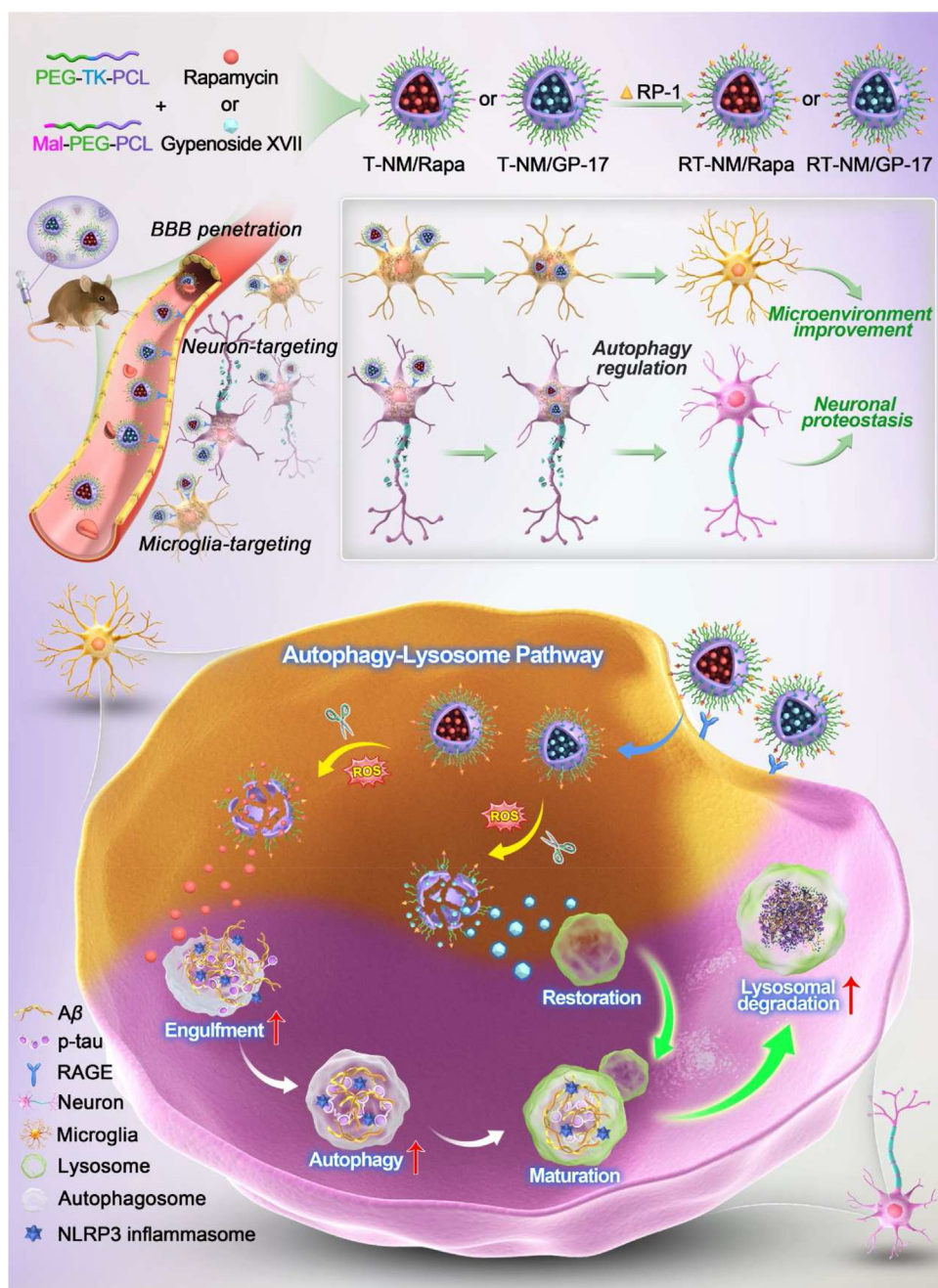


Figure 1 Schematic diagram of co-therapeutic micelle, RT-NM/(Rapa + GP-17), regulating autophagy-lysosome pathway for AD treatment. RT-NM/(Rapa + GP-17) is composed of monotherapeutic micelles, RT-NM/Rapa and RT-NM/GP-17. Mediated by selective RAGE binding of RP-1 peptide, RT-NM/(Rapa + GP-17) can effectively penetrate through blood–brain barrier (BBB) and further target neurons and microglia in Alzheimer’s disease (AD) lesions. Then the micelles with reactive oxygen species (ROS)-responsive thioketal (TK) moiety exhibit efficient intracellular release of rapamycin and gypenoside XVII to activate autophagy and improve lysosomal function, respectively. RT-NM/(Rapa + GP-17) enhances autophagy flux (the entire process of autophagosome formation and autophagic degradation), thereby decreasing aberrant protein burden and relieving neuroinflammation, consequently achieving dual-neuroprotection for AD treatment.

Gypenoside XVII (GP-17) was attained from Push Biotechnology Co., Ltd. (Chengdu, China). RP-1 (CAPDTKTQ) and A β_{1-42} were synthesized by Guotai Biotechnology Co., Ltd. (Hefei, China) and Chinese Peptide Co., Ltd. (Hangzhou, China), respectively. 1,1'-Dioctadecyl-3,3,3',3'-tetramethylindocarbocyanine perchlorate (DiI), 3,3'-dioctadecyloxycarbocyanine perchlorate (DiO), Cell Counting Kit-8 (CCK-8), Total ROS assay kit and BCA Protein

Assay Kit were purchased from Beyotime Biotechnology Co., Ltd. (Shanghai, China). Amyloid- β_{1-40} Human ELISA Kit and Amyloid- β_{1-42} Human ELISA Kit were purchased from Elabscience Biotechnology Co., Ltd. (Shanghai, China). LysoTracker Red DND-99 and LysoSensor Yellow/Blue dextran were purchased from Thermo Fisher Scientific, Inc. (Eugene, OR, USA). The mouse brain microvascular endothelial cells (bEnd.3), mouse hippocampal

neuronal cells (HT22), and murine neonatal microglial cells (BV2) were obtained from the Chinese Academy of Sciences Cell Bank (Shanghai, China). All chemicals used were analytical or reagent grade.

2.2. Cell culture and animals

HT22 cells, BV2 cells and bEnd.3 cells were cultured in DMEM (Gibco, USA) containing 10% FBS (Gibco, Australia), 1% Pen-Strep (100X, Gibco, USA) and 1% Non-Essential Amino Acids (100X, Gibco, USA) at 37 °C in a humidified 5% CO₂ incubator.

Triple-transgenic AD (3 × Tg-AD) mice (B6; 129-Tg (APP^{Swe}, tauP301L)ILfa Psen 1^{tm1Mpm}/Mmjax, male and female in half) were obtained from the Jackson Laboratory (Bar Harbor, ME, USA). Age- and gender-matched wild-type (WT) mice were purchased from Shanghai Model Organisms Center (Shanghai, China). All mice were bred in specific pathogen-free conditions with 12 h light/dark circles, constant temperature at 23 ± 1 °C, and relative humidity at 55 ± 5%. All experimental procedures were executed according to the protocols approved by Institutional Animal Care and Use Committee (IACUC), School of Pharmacy, Fudan University (No. 2020-04-YJ-ZQZ-01).

2.3. Preparation and characterization of micelles

Micelles were prepared *via* solvent diffusion method. PEG-TK-PCL or PEG-PCL (7 mg) and Mal-PEG-PCL (3 mg) were dissolved in acetone (4 mL) with Rapa or GP-17 (0.5 mg, 5% mass ratio of polymeric materials). The mixture was then rapidly injected into stirring distilled water (10 mL), followed by 1 h continuous stirring at 400 r/min. The acetone and unencapsulated drugs were successively removed by rotary evaporation and sepharose CL-4B gel filtration to obtain micelles. The almost same preparation procedure was applied in the preparation of fluorescent probe-loaded micelles (Cou-6, DiR, or DiO/DiI) with the replacement of drugs by fluorescent probes (0.04 mg, 0.4% mass ratio of polymeric materials). For targeted micelles, the targeting ligand, RP-1 peptide, was covalently conjugated on the surface of micelles by Mal-thiol coupling reaction under nitrogen at room temperature for 4 h. The reaction molar ratios of 1:2 and 1:1 (RP-1: Mal-) corresponded to the modification density of 15% and 30%, respectively.

The particle size and zeta potential of the micelles were measured by Zetasizer Nano ZS (Malvern Instruments, Malvern, UK). The morphology of micelles was characterized by JEM-1230 transmission electron microscope (TEM, JEOL, Japan). Drug-loading capacity (DL, %) and encapsulation efficiency (EE, %) of the micelles were analyzed by HPLC (Supporting information).

2.4. ROS-mediated release of drugs

RT-NM/Rapa, R-NM/Rapa, RT-NM/GP-17, and R-NM/GP-17 were transferred to dialysis bags and then immersed in PBS release buffer containing 0.5% SDS and 0 or 1 mmol/L H₂O₂. The samples were incubated at 37 °C with 100 r/min shaking for 48 h. At predetermined time points, 200 µL of samples were collected for HPLC analysis and the same volume of fresh release medium was replenished. The cumulative release of Rapa or GP-17 from micelles at each time point was calculated.

Furthermore, the intracellular drug release of micelles was investigated *via* FRET imaging. R-NM/(DiO/DiI) and RT-NM/(DiO/DiI) were prepared as abovementioned. HT22 cells seeded

in polylysine-coated confocal dishes were treated with regular DMEM containing 100 µmol/L H₂O₂ for 4 h to construct a high-ROS neuronal model. Washed several times with PBS, the cells were then incubated with R-NM/(DiO/DiI) or RT-NM/(DiO/DiI) (50 ng/mL DiO) at 37 °C for 30 min. After the complete removal of un-uptaken micelles, the cells were cultured in fresh regular DMEM for another 0 and 1 h, followed by fixation with 4% paraformaldehyde and nuclei staining with DAPI. The cells were imaged by LSM 710 Confocal Microscope (Carl Zeiss, Germany).

2.5. In vivo evaluation of central neuron and microglia targeting

Mouse cranial windows were prepared on 14-month-old 3 × Tg-AD mice according to previously established protocols²⁷. In brief, mice were anesthetized with 1.5%–3% isoflurane (RWD life science, China) and immobilized using a custom-made fixator. After the removal of hair and skin covering the skull, a craniotomy was performed directly above the somatosensory cortex using a high-velocity micro drill (Strong, Korea). Then the exposed cortical region was covered by a sterile cover glass (Citotest, China) which was affixed with dental cement. 3 × Tg-AD mice with cranial windows were administered with RT-NM/Cou-6 (1 mg Cou-6/kg) *via* tail vein injection. *In vivo* imaging of micelle distribution in the brain parenchyma and vasculature was performed using a two-photon excitation wavelength of 960 nm at a depth of 300 µm below the cortical surface. Images within a spatial range of 50 µm above and below the 300 µm position were captured by Z-axis scanning at 30 min post-injection. The acquisition and processing of images and videos were completed by a multiphoton microscope (FV1200, Olympus, Japan) equipped with a mode-locked Maitai two-photon laser (Spectra Physics, USA) and a 20X water immersion objective (Olympus, Japan), and FV10-ASW software, respectively.

14-month-old 3 × Tg-AD mice were intravenously injected with RT-NM/Cou-6 or T-NM/Cou-6 (0.5 mg Cou-6/kg). One hour later, the mice were anesthetized and perfused with saline and 4% paraformaldehyde. After 48 h fixation in 4% paraformaldehyde and gradient dehydration with sucrose solution, the collected brains were embedded in Tissue-Tek O.C.T (Sakura Finetek, USA) and cut into 10-µm sections. Subsequently, the sections were perforated with 0.3% Triton X100 for 10 min, blocked with Immunol Staining blocking buffer at 37 °C for 1 h, and incubated with anti-NeuN antibody (Abcam, 1:200), anti-Iba1 antibody (Abcam, 1:100) or anti-GFAP antibody (Abcam, 1:200) at 37 °C for 1 h, respectively. The sections were then carefully washed with PBS to remove unbound primary antibodies, and further incubated with the corresponding secondary antibody (Goat anti-rabbit IgG H&L Alexa Fluor 594, Abcam, 1:200) at 37 °C for 1 h. Mounted by coverslips with mounting medium containing nuclear dye DAPI, the sections were visualized under SpinSR10 Spinning Disk Confocal Microscope (Olympus, Japan). The calculation of neuron- or microglia-specific efficiency was performed by ImageJ software as previously described²⁸.

2.6. Investigation of lysosome function

HT22 cells were inoculated into 24-well plates with cell climbing slices and cultured overnight. Pretreated with 2.5 µmol/L Aβ₁₋₄₂ for 24 h, HT22 cells were incubated with RT-NM/Rapa, RT-NM/GP-17, R-NM/(Rapa + GP-17) and RT-NM/(Rapa + GP-17) (100 nmol/L Rapa, 500 nmol/L GP-17), respectively. The slices

were rinsed with PBS, fixed in 4% paraformaldehyde, and then co-incubated with anti-LAMP1 antibody (Abcam, 1:100) and anti-Galectin3 antibody (Abcam, 1:500), followed by the fluorescence labeling with Goat anti-rabbit IgG H&L AF594 (Abcam, 1:200) and Goat anti-mouse IgG H&L AF488 (Abcam, 1:200). The slices were pasted onto slides with mounting medium containing DAPI and observed under LSM 710 Confocal Microscope (Carl Zeiss) for the evaluation of lysosomal membrane permeability. The corresponding Pearson's correlation coefficient (R) of LAMP1 and Galectin3 signals was analyzed by ImageJ software. The slices were also immunostained with anti-TFEB antibody (Proteintech, 1:100) and then fluorescence labeled with Goat anti-rabbit IgG H&L AF594 (Abcam, 1:200) to observe TFEB nuclear translocation.

For the measurement of lysosomal pH, HT22 cells were loaded with 1 mg/mL LysoSensor Yellow/Blue dextran for 24 h at 37 °C after the 24 h pre-incubation with 2.5 $\mu\text{mol/L}$ $A\beta_{1-42}$ and various formulations. The cells were washed three times in PBS, trypsinized, and transferred into a black 96-well microplate. The standard curve was obtained according to the protocol established by Lee et al.²⁹. In brief, cells were treated with 10 $\mu\text{mol/L}$ monensin and 10 $\mu\text{mol/L}$ nigericin in MES buffer (5 mmol/L NaCl, 115 mmol/L KCl, 1.3 mmol/L MgSO_4 , 25 mmol/L Mes), with the pH adjusted to a range from 3.5 to 5.5. The emission at 440 nm and 535 nm with excitation at 355 nm were read by Multiskan Mk3 microplate reader (Thermo Fisher, USA). The ratio of emission, 440/535, was calculated and substituted into the standard curve for pH value determination.

2.7. Evaluation of autophagy-lysosome pathway

The autophagic- and lysosomal-related proteins were tested by Western blotting analysis. HT22 or BV2 cells were exposed to 2.5 $\mu\text{mol/L}$ $A\beta_{1-42}$ for 24 h and then treated with various formulations (100 nmol/L Rapa, 500 nmol/L GP-17) for an additional 24 h. Whereafter, the cells were lysed in RIPA buffer containing a cocktail of protease inhibitors and centrifuged to get supernatant as protein samples. The extracted protein samples were normalized in concentration before the addition of SDS-PAGE Sample Loading Buffer (Beyotime, China) and denaturation. The samples with equal amount of protein were separated on 10% SDS-polyacrylamide gel (15% for LC3 protein), transferred to pre-activated PVDF membranes, and blocked in TBS buffer containing 5% skim milk. Subsequently, the attained protein bands were immunoblotted with primary antibodies and corresponding secondary antibodies. The used antibodies were as followed: anti-Beclin1 antibody (Abcam, 1:1000), anti-LC3B antibody (Abcam, 1:3000), anti-SQSTM1/p62 antibody (Abcam, 1:5000), anti-Cathepsin D antibody (Abcam, 1:2000), anti-LAMP1 antibody (Abcam, 1:1000), anti-GAPDH antibody (Abcam, 1:5000), HRP-conjugated Goat Anti-Rabbit IgG H&L (Abcam, 1:5000) and HRP-conjugated Goat Anti-Mouse IgG H&L (Abcam, 1:5000).

The cultured HT22 cells were pre-stimulated with 2.5 $\mu\text{mol/L}$ $A\beta_{1-42}$ for 24 h, following the further 24 h incubation with various preparations. And then the cells were immunostained by anti-LAMP1 antibody (Abcam, 1:100) and anti-LC3B antibody (Abcam, 1:100), and fluorescently probed with Goat anti-rabbit IgG H&L AF488 (Abcam, 1:200) and Goat anti-mouse IgG H&L AF594 (Abcam, 1:200). The fusion of autophagosome and lysosome was examined under LSM 710 Confocal Microscope (Carl Zeiss). The corresponding Pearson's correlation coefficient (R) of LAMP1 and LC3B signals was analyzed by ImageJ.

2.8. Detection of $A\beta$ clearance

HT22 cells were plated in confocal dishes and co-treated with 2.5 $\mu\text{mol/L}$ $A\beta_{1-42}$ and various micelles (100 nmol/L Rapa, 500 nmol/L GP-17) for 24 h. Afterward, the cells were incubated with medium containing 2 $\mu\text{g/mL}$ FAM- $A\beta_{1-42}$ which was completely discarded 3 h later, and then cultured in fresh DMEM medium for extra 0, 6, or 24 h. The lysosome and nucleus were dyed with LysoTracker Red DND-99 and Hoechst 33342, respectively. Images were captured by SpinSR10 Spinning Disk Confocal Microscope (Olympus) to detect the intracellular $A\beta_{1-42}$ clearance in HT22.

To estimate microglia phagocytosis of extracellular $A\beta$, BV2 cells were co-treated with 2.5 $\mu\text{mol/L}$ $A\beta_{1-42}$ and various micelles (100 nmol/L Rapa, 500 nmol/L GP-17) for 24 h, and then incubated with 2 $\mu\text{g/mL}$ FAM- $A\beta_{1-42}$ for 3 h. Following lysosome staining with LysoTracker Red DND-99 and nuclei staining with Hoechst 33342, the cells were observed under LSM 710 Confocal Microscope (Carl Zeiss). The FAM- $A\beta_{1-42}$ fluorescence intensity of BV2 cells was also analyzed via CytoFlex S flow cytometer (Beckman Coulter, USA).

2.9. Assessment of neuroinflammation

After the indicated 24 h treatment with $A\beta_{1-42}$, BV2 cells were treated with various formulations (100 nmol/L Rapa, 500 nmol/L GP-17) for 24 h. The protein samples were harvested as previously aforementioned. Western Blotting analysis was then performed to evaluate the expression of neuroinflammation-associated proteins. The used antibodies were as followed: anti-NLRP3 antibody (Abcam, 1:1500), anti-Caspase1 antibody (Abcam, 1:1000), anti-GAPDH antibody (Abcam, 1:5000), and HRP-conjugated Goat Anti-Rabbit IgG H&L (Abcam, 1:5000).

2.10. Animal treatment and experiment design

14–15-month-old $3 \times \text{Tg-AD}$ mice were randomly divided into five groups ($n = 9$). Age- and gender-matched wild-type mice served as the normal control group. The group setting was as follows: WT group (saline), AD group (saline), RT-NM/Rapa group (0.05 mg Rapa/kg/d), RT-NM/GP-17(L) group (0.375 mg GP-17/kg/d), RT-NM/GP-17(H) group (1.5 mg GP-17/kg/d), and RT-NM/(Rapa + GP-17) group (RT-NM/Rapa, 0.05 mg Rapa/kg/d and RT-NM/GP-17, 0.375 mg GP-17/kg/d). The continuous 28-day intravenous administration was performed according to this dosage regimen.

2.11. Morris water maze (MWM) experiment

The cognitive ability of $3 \times \text{Tg-AD}$ mice was evaluated by the MWM on the 22nd day of treatment. The MWM consisted of two parts, spatial navigation task and probe trial test. In the spatial navigation task, mice received a consecutive 6-day training for submerged platform seeking. Each mouse received four-time repeated training according to the randomly-determined training quadrant sequence every day. If the mice successfully found the platform in 60 s with a 5-s stay, the searching time was recorded as escape latency, otherwise, the cut-off time, 60 s, was taken as escape latency and the mice were manually led for a 10-s dwell on the platform as supplementary training. After the spatial navigation task, the platform was removed and the probe trial test was conducted. The mice were allowed a 60-s free swim which started

in the farthest quadrant from the original platform location. The swimming trajectories were tracked and analyzed by Water maze video-track system (Coulbourn, USA).

2.12. Morphological observation of lysosome

Subsequent to cardiac perfusion with saline and 2.5% glutaraldehyde PB buffer, 1 mm³ of brain tissue in the hippocampus was dissected and further fixed in 4% paraformaldehyde and 2.5% glutaraldehyde PB buffer at 4 °C overnight. Then the brain tissue underwent the dehydration of gradient ethanol, the replacement of propylene oxide and the immersion in Epon812 embedding solution. After 48 h drying at 60 °C, the ultrathin sections were prepared and stained by lead citrate. The morphology of lysosome was observed by transmission electron microscope (H-7650, HITACHI, Japan).

2.13. Enzyme-linked immunosorbent assay (ELISA) of A β ₁₋₄₀ and A β ₁₋₄₂

After the homogenization in RIPA buffer containing a cocktail of protease inhibitors, the harvested brain homogenates were completely lysed under constant 1 h agitation and then centrifuged at 10,000 × *g* (Biofuge stratos, Thermo Fisher, Germany) for 20 min at 4 °C. The supernatants were collected as soluble fractions. The centrifugal precipitates were further sonicated in 70% (*w/v*) formic acid, followed by centrifugation at 10,000 × *g* (Biofuge stratos, Thermo Fisher, Germany) for 30 min at 4 °C. The supernatants neutralized by 1 mol/L Tris Buffer were retrieved as insoluble fractions. Thereafter, the levels of A β ₁₋₄₀ and A β ₁₋₄₂ in soluble and insoluble fractions were determined in accordance with the operating instructions of Amyloid- β 1-40 Human ELISA Kit and Amyloid- β 1-42 Human ELISA Kit (Elabscience, China), respectively.

2.14. Real-time quantitative PCR

The total RNA was extracted from brain tissues with ice-cold Trizol (Invitrogen, USA), and then reverse-transcribed into cDNA using Hifair II first strand cDNA synthesis kit (Yeasen, China). Following the directions of qPCR SYBR Green Master Mix kit (Yeasen, China), the cDNA samples were amplified on QuantStudio3 (Appliedbiosystems, USA). The relative expression of target gene was calculated *via* the 2^{- $\Delta\Delta C_t$} method with β -actin as the internal reference. The primers used are listed in [Supporting Information Table S1](#).

2.15. Immunohistochemistry analysis

The brain tissues were fixed in 4% paraformaldehyde, dehydrated in ascending series of ethanol, cleared in xylene and then embedded in paraffin. The paraffin-embedded brains were sectioned into 8- μ m coronal slices. The immunohistochemical staining was performed on the routine method. Briefly, prior to immunolabeling, the following operations were done sequentially, including xylene dewaxing, gradient ethanol hydration, antigen retrieval with citrate buffer, and blocking with QuickBloc blocking buffer (Beoyotime, China). The sections were further incubated with primary antibody, anti-A β ₁₋₄₂ antibody (Biolegend, 1:50) or anti-Phospho-tau (Ser202, Thr205) antibody (Thermo Fisher, 1:100), at 4 °C overnight, followed by the incubation with HRP-conjugated Goat anti-mouse IgG (Abcam, 1:200) at 37 °C

for 1 h. After being stained with DAB reagent and counterstained with hematoxylin solution, the sections were dehydrated by ethanol gradients, cleared in xylene, and coverslipped with neutral resin. The prepared sections were observed by microscope (Leica DMI 4000B, Germany) and the percentage area of amyloid plaque deposit was quantitatively analyzed by ImageJ software.

2.16. Nissl staining

The paraffin sections were first deparaffinized and hydrated and then stained with Nissl staining solution, followed by dehydration in ethanol gradients and clearance in xylene. The stained sections were sealed with neutral balsam for observation under the microscope.

2.17. Statistical analysis

All data were presented in the form of mean \pm SD unless otherwise stated. Statistical significance was calculated by student's *t*-test in a two-group comparison or by one-way ANOVA analysis combined with Dunnett's *post hoc* test in a multi-group comparison. The statistical significance was set at *P* < 0.05.

3. Results

3.1. Preparation and characterization of drug-loaded micelles

The polymer material PEG-TK-PCL, containing ROS-cleavable thioketal (TK) bond in the backbone, was synthesized through the condensation of TK-containing diacid and amine (NH₂)-terminated polymers ([Supporting Information Fig. S2](#)). The presence of TK in the polymer was confirmed by the ¹H nuclear magnetic resonance (¹H NMR) spectrum which showed characteristic proton peaks attributed to the thioketal linker (–CH₃ proton peaks at ~1.67 ppm and –CH₂– proton peaks at both 2.89 ppm and 2.48–2.63 ppm) ([Supporting Information Fig. S3](#)). The critical micelle concentration (CMC) of PEG-TK-PCL was estimated to be 6.139 μ g/mL ([Fig. 2A](#)), indicating its ability to form micelles at an extremely low concentration.

ROS-responsive micelles (T-NM) were prepared by the solvent diffusion method with ROS-sensitive PEG-TK-PCL and maleimide-PEG-PCL (Mal-PEG-PCL) in a 7:3 mass ratio. The RP-1 peptide was then anchored to the surface of micelles *via* the thiol-Mal Michael addition reaction. To optimize the targeting capability, the RP-1 modification density was screened by *in vitro* cellular uptake and mouse *ex vivo* imaging ([Supporting Information Fig. S4](#)). The RP-1-conjugated T-NM (RT-NM) with 30% RP-1 modification density displayed the highest uptake in A β ₁₋₄₂-pretreated bEnd.3 cells (mouse cerebral microvascular endothelial cells), HT22 cells (mouse hippocampal neuronal cells), and BV2 cells (mouse microglia). Meanwhile, 30% RT-NM exhibited notably increased BBB penetration in 3 × Tg-AD mice, making it the optimum density. As a control, RP-1-modified non-ROS-responsive micelles (R-NM) were prepared using PEG-PCL instead of PEG-TK-PCL.

The characterization of micelle systems was shown in [Fig. 2B](#). The mean particle sizes of Rapa-encapsulated or GP-17-loaded micelles were around 48 nm and 46 nm, respectively. Although both Rapa and GP-17 could be entrapped effectively in RT-NM, there was a gap of approximately 20% between their encapsulation efficiencies (90% for Rapa and 73% for GP-17) due to the

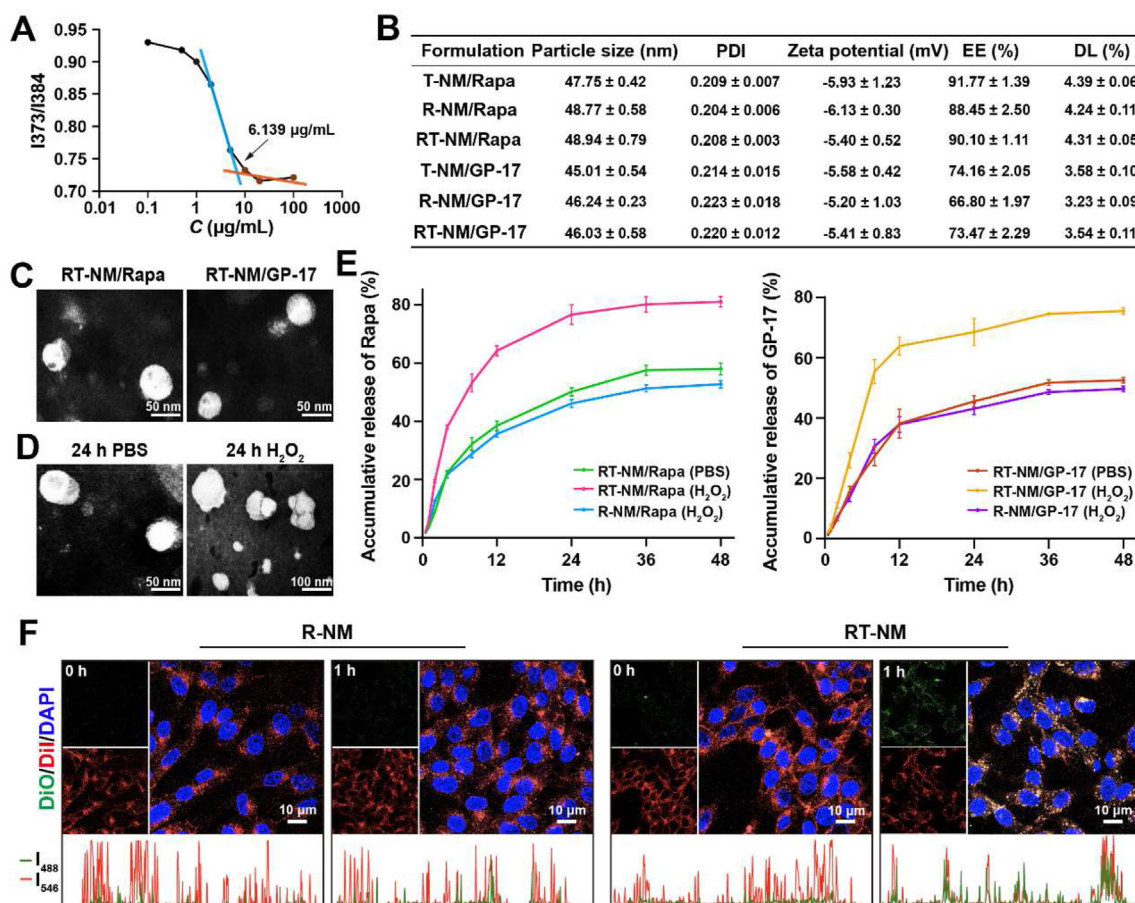


Figure 2 Micelle characterization and ROS-responsive release. (A) Curve diagram of pyrene emission spectra intensity ratio I373/I384 versus PEG-TK-PCL concentration. (B) Particle size, polydispersity index (PDI), zeta potential, encapsulation efficiency (EE) and drug loading (DL) of T-NM/Rapa, R-NM/Rapa, RT-NM/Rapa, T-NM/GP-17, R-NM/GP-17, and RT-NM/GP-17. T-NM, non-RP-1-modified ROS-responsive micelle; R-NM, RP-1-modified non-ROS-responsive micelle; RT-NM, RP-1-modified ROS-responsive micelle ($n = 3$). (C) Morphological characterization of RT-NM/Rapa and RT-NM/GP-17 *via* transmission electron micrograph. Scale bar = 50 nm. (D) Morphological change of RT-NM after incubation in PBS buffer (pH 7.4) with or without 1 mmol/L H_2O_2 at 37 °C for 24 h. Scale bar = 50 or 100 nm. (E) *In vitro* release of Rapa and GP-17 from RT-NM and R-NM in PBS buffer (pH 7.4) with or without 1 mmol/L H_2O_2 at 37 °C for 48 h ($n = 3$). (F) Representative fluorescence images and quantitative analysis of fluorescent intensity of H_2O_2 -pretreated HT22 cells after incubation with DiO/DiI-loaded R-NM and RT-NM at 37 °C. Scale bar = 10 μ m. (B, E) Data are expressed as mean \pm SD.

difference in physicochemical properties, making it difficult to realize the controllable co-loading of these two drugs. And the separated-loading was demonstrated as a satisfactory combination mode in nano-combination therapy with superior therapeutic benefits in our previous study³⁰. Hence, separated-loading was chosen for the follow-up research. Transmission electron microscopy (TEM) images depicted the spherical morphology of RT-NM with uniform size and good dispersibility (Fig. 2C). The biocompatibility of PEG-PCL was not negatively influenced by the insertion of TK, as the viabilities of HT22 cells and BV2 cells both exceeded 80% after 24 h incubation with blank R-NM or RT-NM at concentrations up to 2 mg/mL (Supporting Information Fig. S5). RT-NM remained stable even after 40-fold dilution with PBS or 10% fetal bovine serum (FBS) at 37 °C for 24 h (Supporting Information Fig. S6).

3.2. ROS-responsiveness of RT-NM

Since cellular ROS concentration is up to 1 mmol/L during oxidative stress³¹, PBS containing 1 mmol/L H_2O_2 was utilized to simulate the

high ROS environment in cells. After 24 h incubation, RT-NM experienced ROS-triggered disassembly, which was confirmed by obvious morphological changes in TEM images, including increased size, irregular shape and appearing small fragments. By contrast, no visible alteration was observed when incubated with PBS (Fig. 2D). Moreover, the exposure to H_2O_2 accelerated the drug release of RT-NM and enhanced the 48 h cumulative release percentages by 1.53- and 1.52-fold for RT-NM/Rapa and RT-NM/GP-17, respectively, compared with non-responsive micelles (R-NM), indicating that RT-NM could realize fast and sufficient drug release under oxidative environment (Fig. 2E).

For the assessment of intracellular ROS-triggered release of RT-NM, fluorescence resonance energy transfer (FRET) effect of RT-NM/(DiO/DiI) was monitored in oxidative stress cell model, H_2O_2 -pretreated HT22 cells (Fig. 2F). At 0 h, only strong DiI signals (red) were observed in both RT-NM and R-NM groups, that was, there existed substantial FRET effects (quenched DiO, activated DiI) which were produced by the extreme proximity of DiO and DiI, implying that the micelles were internalized intactly

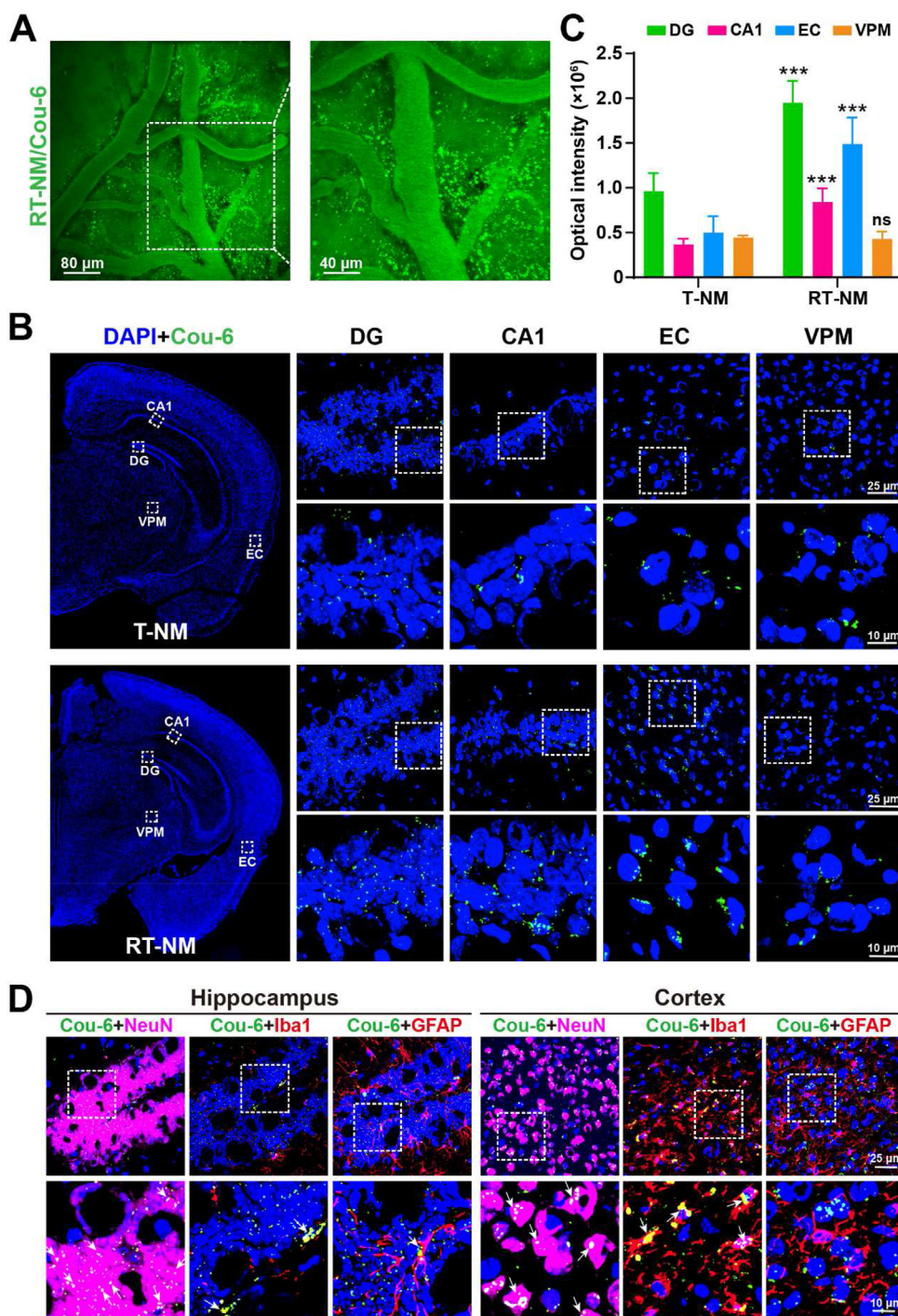


Figure 3 Targetability of RT-NM. (A) Two-photon microscopy images of RT-NM/Cou-6 across the cerebral vessels of $3 \times$ Tg-AD mice at 30 min post-injection (1 mg Cou-6/kg). Scale bar = 80 or 40 μm . (B) Representative confocal images of T-NM/Cou-6 or RT-NM/Cou-6 distribution in different brain regions of $3 \times$ Tg-AD mice at 1 h post-injection (0.5 mg Cou-6/kg). DG, dentate gyrus; EC, entorhinal cortex; VPM, ventral posterior medial thalamic nucleus. Scale bar = 25 or 10 μm . (C) Quantitative analysis of fluorescent intensity of T-NM/Cou-6 or RT-NM/Cou-6 in different brain regions ($n = 6$). Data were presented as mean \pm SD. *** $P < 0.001$; ns, not significant; compared with the corresponding region of T-NM. (D) Representative confocal images of cell population tropism of RT-NM/Cou-6 in hippocampus or cortex of $3 \times$ Tg-AD mice at 1 h post-injection (0.5 mg Cou-6/kg). Neuron, stained with NeuN antibody (purple); Microglia, stained with Iba1 antibody (red); Astrocyte, stained with GFAP antibody (red). White arrows represent micelles colocalized with cells. Scale bar = 25 or 10 μm .

by HT22 cells. At 1 h, observable DiO signals (green) occurred and DiI signals weakened in the RT-NM group, representing the diminishment of FRET effect owing to the increased distance between DiO and DiI caused by their release from RT-NM.

However, the R-NM group still presented obvious FRET effect, suggesting that most DiO/DiI was unreleased from R-NM within 1 h. These results demonstrated that RT-NM could release drugs faster in response to the high intracellular ROS.

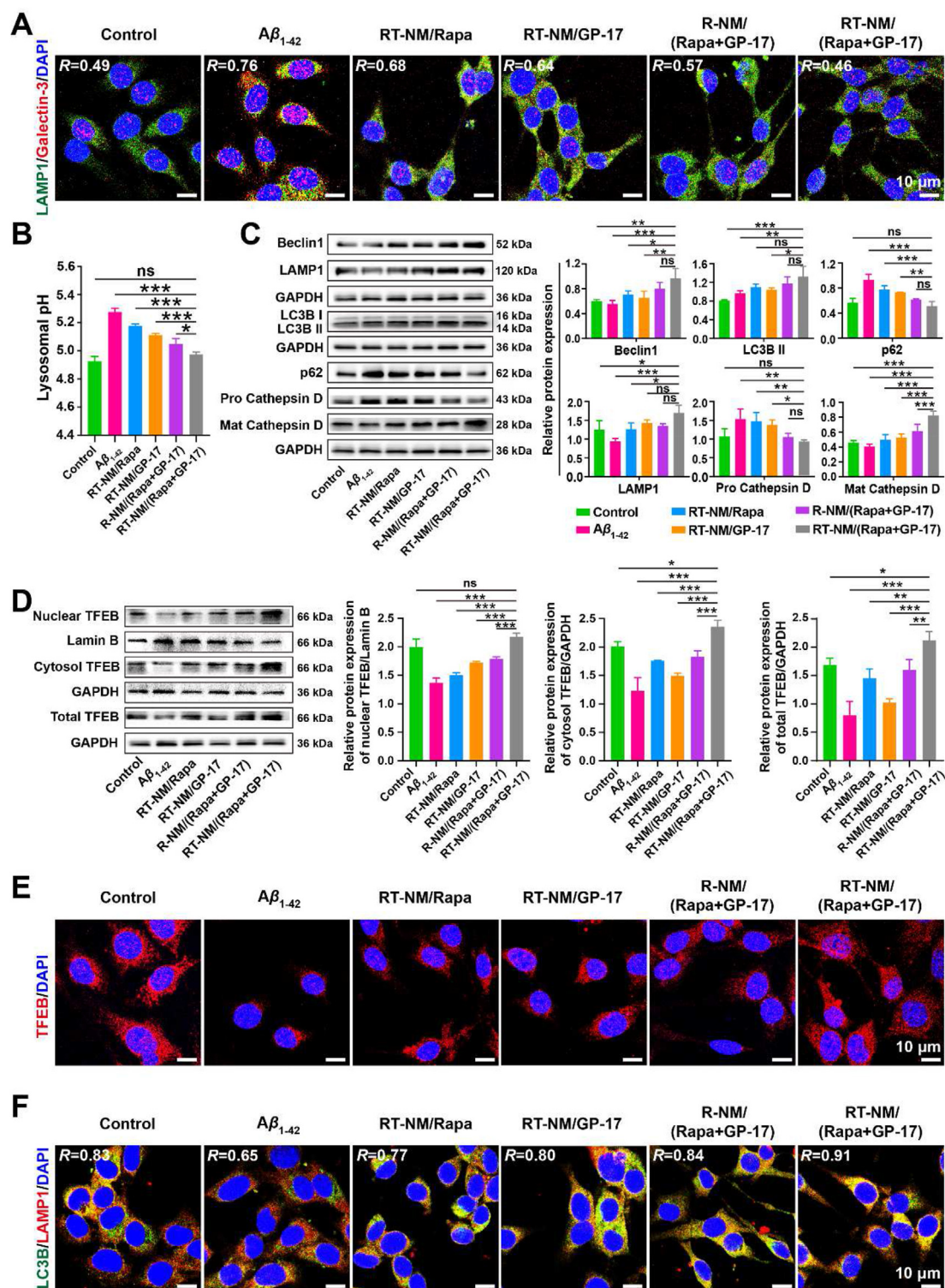


Figure 4 Regulation of the entire autophagy-lysosome pathway by RT-NM/(Rapa + GP-17) *in vitro*. (A–F) HT22 cells were preincubated with $A\beta_{1-42}$ (2.5 $\mu\text{mol/L}$) and then treated with RT-NM/Rapa, RT-NM/GP-17, R-NM/(Rapa + GP-17) or RT-NM/(Rapa + GP-17) (100 nmol/L Rapa, 500 nmol/L GP-17) for 24 h. (A) Representative confocal images of HT22 cells immunostained by LAMP1 antibody (green), Galectin-3 antibody (red), and DAPI (blue). Scale bar = 10 μm . Pearson's correlation coefficient (R) was calculated by Image J. (B) Lysosomal pH levels of HT22 cells detected by Lysosensor Yellow/Blue-dextran ($n = 3$). (C) Levels of autophagic- and lysosomal-related proteins of HT22 cells analyzed by Western blotting ($n = 3$). (D) Expression of TFEB in nuclear and cytosol fraction, and total TFEB in cell lysates of HT22 cells determined by Western blotting ($n = 3$). (E) Representative confocal images of HT22 cells immunostained by TFEB antibody (red) and DAPI (blue). Scale bar = 10 μm . (F) Representative confocal images of HT22 cells immunostained by LC3B antibody (green), LAMP1 antibody (red), and DAPI (blue). Scale bar = 10 μm . Pearson's correlation coefficient (R) was calculated by Image J. (B–D) Data were presented as mean \pm SD. * $P < 0.05$, ** $P < 0.01$, *** $P < 0.001$; ns, not significant; compared with RT-NM/(Rapa + GP-17) group.

3.3. Central neuron and microglia targeting ability of RT-NM

The targetability of the micelles was probed by coumarin-6 (Cou-6), a commonly used fluorescent probe for *in vivo* nano-system tracking^{32,33}. Under two-photon microscopy, it was found that RT-NM achieved efficient permeation across the cerebral vessels in $3 \times$ Tg-AD mice (Fig. 3A, Supporting Information Movie S1). The distribution of RT-NM in brain parenchyma was then observed at 1 h post-injection. Results showed that RP-1 modification increased the concentration of micelles in regions vulnerable to AD pathologies, such as the dentate gyrus (DG), CA1 area of hippocampus, and entorhinal cortex (EC)³⁴, with 2.03-, 2.29-, and 2.98-fold higher fluorescence intensity, respectively, compared to non-targeted micelles (T-NM). However, the ventral posterior medial nucleus in thalamus (VPM), an area less affected by AD, showed similar fluorescence intensity between T-NM and RT-NM groups, demonstrating that RP-1 modification conferred lesion-selectivity to RT-NM (Fig. 3B and C). Immunofluorescence analysis of brain sections stained with NeuN (neuron marker), Iba1 (microglia marker), and GFAP (astrocyte marker) further revealed that RT-NM selectively targeted neuron and microglia, with 1.21-fold (in hippocampus) and 2.13-fold (in EC) higher neuron-targeting specificity and 2.56-fold (in hippocampus) and 2.25-fold (in EC) higher microglia-targeting specificity than T-NM (Fig. 3D and Supporting Information Fig. S7). Collectively, RP-1-modified micelles efficiently penetrated BBB and targeted neurons and microglia in AD lesions.

Supplementary video related to this article can be found at <https://doi.org/10.1016/j.apsb.2023.10.009>

3.4. Regulation of the entire autophagy-lysosome pathway by RT-NM/(Rapa + GP-17) *in vitro*

RT-NM/(Rapa + GP-17) was designed to regulate the entire autophagy-lysosome pathway *via* the combination of lysosomal remediation and autophagy induction. AD-associated lysosomal impairments have been identified as lysosomal membrane permeabilization, acidification disorder, lysosomal hydrolysis defect, etc³⁵. Since β -galactin-3 can transfer and attach to the surface of lysosomes whose membrane permeability is increased³⁶, the lysosomal membrane permeabilization can be reflected by the colocalization of β -galactin-3 and LAMP1 (lysosome marker). As illustrated in Fig. 4A, there were obvious yellow signals generated by the colocalization of β -galactin-3 (red) and LAMP1 (green) in the $A\beta_{1-42}$ -treated HT22 cells, indicating a serious $A\beta_{1-42}$ -induced lysosomal membrane permeability increment. Noteworthy, the yellow colocalization signals almost disappeared in the RT-NM/(Rapa + GP-17) group with a comparable Pearson's correlation coefficient ($R = 0.46$) to that of the control group ($R = 0.49$), signifying the mitigation of lysosomal membrane permeabilization by RT-NM/(Rapa + GP-17). RT-NM/(Rapa + GP-17) also reversed the abnormally elevated lysosome pH (5.28) caused by $A\beta_{1-42}$ to the normal level (pH = 4.97, Fig. 4B). Meanwhile, RT-NM/(Rapa + GP-17) also efficaciously promoted lysosomal biosynthesis and restored the lysosomal turnover of cathepsin D, which was demonstrated by the upregulated LAMP1 and mature cathepsin D level and the reduced pro cathepsin D level, resulting in improved lysosomal hydrolysis (Fig. 4C). Additionally, the augment of the nuclear and total expression of

TFEB, a critical regulator of lysosomal function and biogenesis, whose transcriptional activity is activated upon nuclear translocation³⁷, explained the mechanism by which RT-NM/(Rapa + GP-17) achieved lysosome regulation (Fig. 4D and E).

To characterize autophagy induction, the levels of autophagic-related proteins were determined by Western blotting (Fig. 4C). Autophagy induction was depressed in the $A\beta_{1-42}$ -treated HT22 cells, as indicated by the decreased level of Beclin 1, the essential protein for autophagy nucleation³⁸, while RT-NM/(Rapa + GP-17) generated strong inductive effects on autophagy with significantly increased Beclin 1 level. And the accumulation of LC3B-II (autophagosome marker) and SQSTM1/p62 (autophagy substrate protein) implied the damaged autophagic degradation of neurons after exposure to $A\beta_{1-42}$. The level of SQSTM1/p62 in the RT-NM/(Rapa + GP-17) group was remarkably lower than that in the other groups, suggesting the greatly improved autophagic degradation by RT-NM/(Rapa + GP-17). Therefore, the increased LC3B-II level in RT-NM/(Rapa + GP-17) group was credited to the accelerated autophagosome assembly rather than its aberrant accumulation.

The fusion of autophagosome and lysosome was detected to further evaluate the patency of autophagy flux (Fig. 4F). The autophagosome and lysosome were fluorescence-labeled with LC3B (green) and LAMP1 (red), respectively. The apparent colocalization of LC3B and LAMP1 was observed in the RT-NM/(Rapa + GP-17) group with the highest Pearson's correlation coefficient, evincing that RT-NM/(Rapa + GP-17) effectively promoted the autophagolysosomal fusion to ensure the patency of autophagy flux.

Similarly, RT-NM/(Rapa + GP-17) also effectually alleviated $A\beta_{1-42}$ -caused dysregulation of autophagy-lysosome pathway in BV2 cells (Supporting Information Fig. S8). Compared to the monotherapeutic micelles (RT-NM/Rapa and RT-NM/GP-17), the co-therapeutic micelles (R-NM/(Rapa + GP-17) and RT-NM/(Rapa + GP-17)), exhibited stronger regulative effects on the autophagy-lysosome pathway in both neuron and microglia, corroborating the superiority of co-intervention in lysosomal function and autophagy induction. And the rapid and sufficient drug release was conducive to the exertion of therapeutic effects, as evidenced by the better performance of RT-NM/(Rapa + GP-17) over R-NM/(Rapa + GP-17).

3.5. Clearance of pathological proteins *in vitro*

The clearance of pathological proteins was then investigated. The intracellular fate of FAM-labeled $A\beta_{1-42}$ (FAM- $A\beta_{1-42}$) in HT22 cells was monitored to explore whether the regulation of autophagy-lysosome pathway by RT-NM/(Rapa + GP-17) could facilitate the lysosomal degradation of $A\beta_{1-42}$ (Fig. 5A and B). The internalized FAM- $A\beta_{1-42}$ scattered in the cytoplasm with rare colocalization with lysosomes in the $A\beta_{1-42}$ -pretreated cells and an additional 24 h culture later, there were still substantial undegraded FAM- $A\beta_{1-42}$, suggesting the vitiated clearance of intracellular $A\beta$. However, the treatment of RT-NM/(Rapa + GP-17) changed the intracellular FAM- $A\beta_{1-42}$ situation, as most FAM- $A\beta_{1-42}$ colocalized with lysosomes and gradually disappeared during the subsequent culture, finally being almost invisible. It was substantiated that RT-NM/(Rapa + GP-17) boosted the autophagic clearance of intraneuronal $A\beta$.

Phagocytosis is closely related to microglial autophagy and crucial for the clearance of extracellular $A\beta$ ^{39,40}. Therefore, the phagocytosis of FAM- $A\beta_{1-42}$ by BV2 cells was observed to

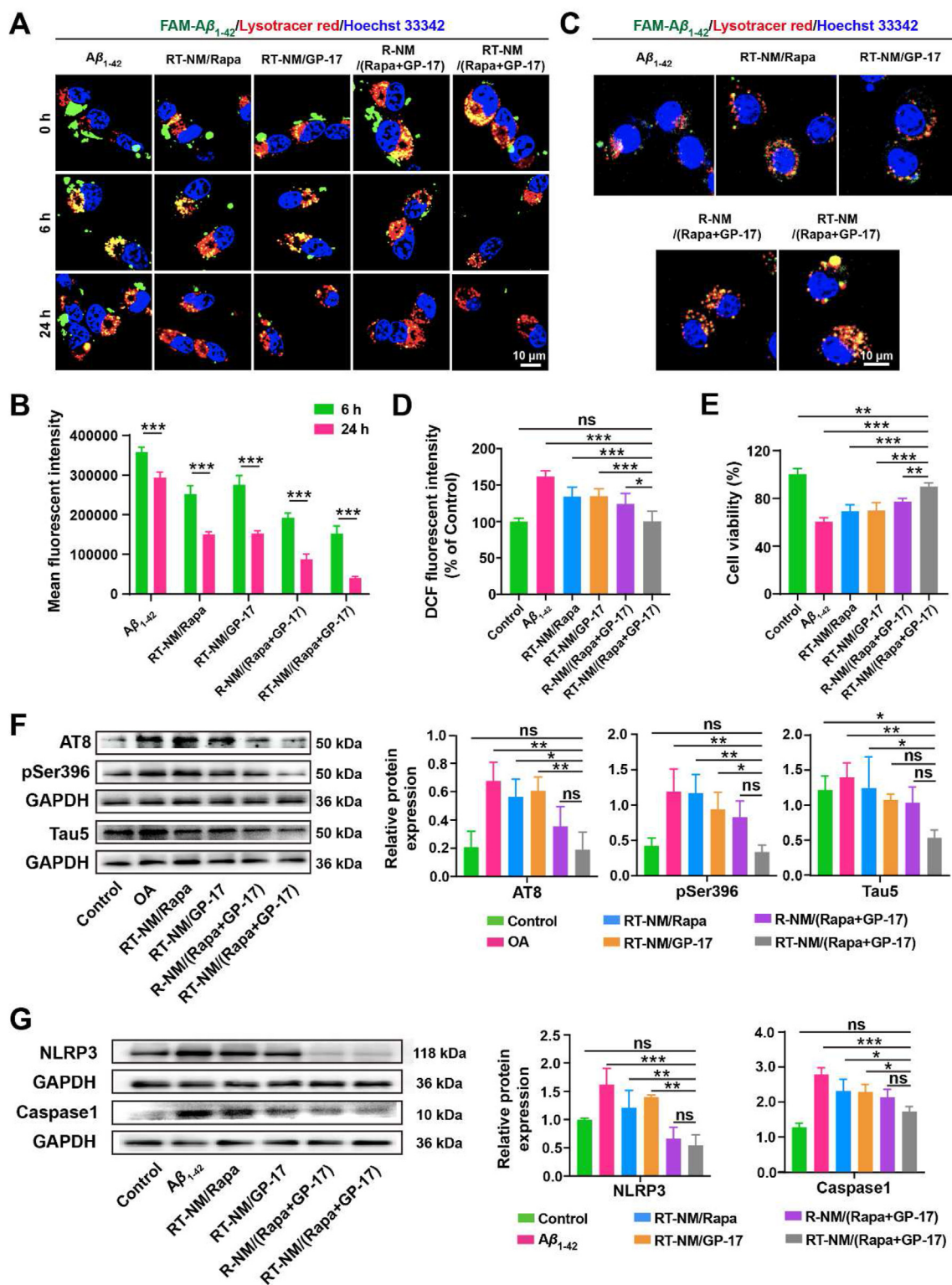


Figure 5 Effects of RT-NM/(Rapa + GP-17) on pathological proteins clearance *in vitro*. (A) Fluorescence monitoring of intracellular fate of FAM- $A\beta_{1-42}$ in HT22 cells. After 24 h preincubation of $A\beta_{1-42}$ (2.5 $\mu\text{mol/L}$) and various formulations (100 nmol/L Rapa, 500 nmol/L GP-17), HT22 cells were treated with FAM- $A\beta_{1-42}$ (2 $\mu\text{g/mL}$) for 3 h and further cultured in blank DMEM medium for 0, 6, and 24 h. FAM- $A\beta_{1-42}$, green; Lysosomes, stained with LysoTracker Red, red; Nuclei, stained with Hoechst 33342, blue. Scale bar = 10 μm . (B) Quantitative analysis of the fluorescence intensity of FAM- $A\beta_{1-42}$ in HT22 cells from Panel A was performed by Image J ($n = 6$). (C) Representative confocal images of FAM- $A\beta_{1-42}$ phagocytosis by BV2 cells. BV2 cells were co-incubated with $A\beta_{1-42}$ (2.5 $\mu\text{mol/L}$) and various preparations (100 nmol/L Rapa, 500 nmol/L GP-17) for 24 h and then treated with FAM- $A\beta_{1-42}$ (2 $\mu\text{g/mL}$) for 3 h. FAM- $A\beta_{1-42}$, green; Lysosomes, stained with LysoTracker Red, red; Nuclei, stained with Hoechst 33342, blue. Scale bar = 10 μm . (D) ROS levels of $A\beta_{1-42}$ -preincubated HT22 cells detected by DCFH-DA probe after 24 h treatment of

investigate the effects of RT-NM/(Rapa + GP-17) on microglia phagocytosis (Fig. 5C and Supporting Information Fig. S9). RT-NM/(Rapa + GP-17) group exhibited the highest green fluorescence intensity of FAM- $A\beta_{1-42}$ and the phagocytosed FAM- $A\beta_{1-42}$ mainly concentrated in lysosomes, manifesting that RT-NM/(Rapa + GP-17) enhanced the microglia phagocytosis of extracellular $A\beta$ and its transport to lysosomes for further clearance.

The accumulation of $A\beta$ is identified as a fatal factor that engenders oxidative stress, neurotoxicity, and ultimate neuron death⁴¹. In view of this, the elimination of $A\beta$ is anticipated to mute its adverse impacts on neurons. As expected, owing to the boosted autophagic scavenging of toxic $A\beta$, RT-NM/(Rapa + GP-17) embodied exceptional neuroprotective effects, corroborated by the rollback of intracellular ROS levels to normal and the rejuvenation of cell viability (Fig. 5D and E). In addition, it is believed that the removal of extracellular $A\beta$ via microglia phagocytosis would amplify the neuroprotective effect of RT-NM/(Rapa + GP-17) *in vivo*.

Apart from $A\beta$, p-tau is in the array of autophagic substrates as well⁴², thus, the autophagic degradation activity on p-tau was also tested. The tau-hyperphosphorylated cell model was established via preincubation with okadaic acid (OA), featuring a significant increase in tau phosphorylation at Ser396 and AT8 (Ser202/Thr205) sites (Fig. 5F). The diseased rise of p-tau levels was inhibited to different degrees by the treatment of various micelles, amidst which, RT-NM/(Rapa + GP-17) showed the most prominent capacity in p-tau clearance with the maximum diminution in p-tau levels. Besides p-tau, RT-NM/(Rapa + GP-17) also promoted the clearance of t-tau (Tau5).

$A\beta$ and p-tau are NLRP3 inflammasome activators, and the overactivated NLRP3 inflammasome, which mediates excessive neuroinflammation, is a potent driver of $A\beta$ pathology and tau pathology^{43,44}. As autophagy is a pivotal pathway for the disposal of NLRP3 inflammasome in microglia, the prompted clearance of NLRP3 inflammasome by virtue of upgraded autophagy flux was further checked (Fig. 5G). The escalating levels of NLRP3 inflammasome components, NLRP3 and Caspase-1, reflected the accumulation of inflammasome in $A\beta_{1-42}$ -treated BV2 cells, which was the joint outcome of $A\beta$ -stimulated inflammasome activation and autophagy deficiency. Satisfactorily, the unwanted inflammasome amassment was assuaged by RT-NM/(Rapa + GP-17) with significantly lowered levels of NLRP3 and Caspase-1, hinting at the attenuation of subsequent pro-inflammatory responses.

3.6. Rescue of spatial memory impairment in triple-transgenic mice by RT-NM/(Rapa + GP-17)

The spatial learning and memory of $3 \times$ Tg-AD mice, a transgenic mouse model possessing both $A\beta$ and tau pathologies⁴⁵, was evaluated via Morris Water Maze (MWM) test on the 22nd day of administration (Fig. 6A). Unlike the wild-type (WT) control whose escape latencies presented a pronounced descending trend during the 6-day training, $3 \times$ Tg-AD mice showed slightly fluctuating escape latencies without significant shortening, suggesting the severely disordered spatial memory in 14–15-month AD mice. Of

note, the amelioration of spatial learning ability at varying degrees happened to AD mice after the treatment with different micelles. Especially, the RT-NM/(Rapa + GP-17)-treated AD mice displayed the maximum curtailment in escape latencies, comparable to that of the WT mice (Fig. 6B). Correspondingly, in the probe trial, the AD mice were inclined to swim aimlessly, whereas the AD mice treated with RT-NM/(Rapa + GP-17) tended to move toward the initial platform location (Fig. 6C). The analysis of swimming paths revealed that among the administration groups, both the highest percentage of time in targeted quadrant and the most platform crossing times occurred in the RT-NM/(Rapa + GP-17) group, proving its prominent therapeutic effects to rescue the impaired spatial memory of AD mice (Fig. 6D).

3.7. Restoration of autophagic flux in triple-transgenic mice by RT-NM/(Rapa + GP-17)

The autophagic flux was characterized through the expression of representative proteins involved in the different links of the autophagy-lysosome pathway. Although the monotherapeutic micelles displayed certain regulative ability on autophagy flux, demonstrated by the altered levels of related proteins, the modulating effects generated by them were inferior to the co-therapeutic micelles, RT-NM/(Rapa + GP-17). The medication of RT-NM/(Rapa + GP-17) induced marked upregulation of Beclin 1, Parkin, LAMP1 and mature cathepsin D, and striking diminishment of p62, suggesting that RT-NM/(Rapa + GP-17) not only activated autophagy but also recovered lysosome functions, consequently enhancing the autophagy flux (Fig. 7A). Additionally, the lysosome state was further observed by TEM. The lysosomes in hippocampal neurons of AD mice visibly swelled, whose average volume increased to 5.9-time of that of WT mice (Fig. 7B). And the number of lysosomes decreased to 51.7% of that in WT mice. These findings proved that lysosomes suffered severe disorders in 14–15-month AD mice. However, RT-NM/(Rapa + GP-17) evidently mitigated the abnormalities of lysosomes, as indicated by the reduced average size and increased number of lysosomes. Altogether, RT-NM/(Rapa + GP-17) effectuated the unblocking of autophagy-lysosome pathway in AD via the co-intervention on autophagy induction and lysosome function.

3.8. Reduction of $A\beta$ burden and tau hyperphosphorylation in triple-transgenic mice by RT-NM/(Rapa + GP-17)

Next, the clearance of $A\beta$ and p-tau *in vivo* was verified. The levels of both soluble and insoluble $A\beta_{1-40}$ and $A\beta_{1-42}$ in the whole brain of AD mice were measured by ELISA. The administration of micelles had positive consequences on the $A\beta$ clearance with declines of varying degrees in $A\beta$ levels. Especially, RT-NM/(Rapa + GP-17) produced a notable reduction in levels of soluble and insoluble $A\beta_{1-42}$, the main pathogenic $A\beta$ isoform, by 41.9% and 42.0% (relative to AD mice), respectively (Fig. 8A). The $A\beta_{1-42}/A\beta_{1-40}$ protein ratio, a more accurate indicator cluing advanced AD deleterious events⁴⁶, was further calculated. The

various preparations ($n = 3$). (E) Cell viability of $A\beta_{1-42}$ -preincubated HT22 cells measured by CCK-8 assay after 24 h treatment of various preparations ($n = 6$). (F) P-tau protein (AT8 and pSer396) and t-tau (Tau5) levels of okadaic acid (OA, 50 nmol/L, 4 h)-pretreated HT22 cells measured by Western blotting after 24 h treatment of various preparations ($n = 3$). (G) Levels of NLRP3 inflammasome components of $A\beta_{1-42}$ -preincubated BV2 cells determined by Western blotting after 24 h treatment of various preparations ($n = 3$). (B, D-G) Data were presented as mean \pm SD. * $P < 0.05$, ** $P < 0.01$, *** $P < 0.001$; ns, not significant; compared between the connected groups.

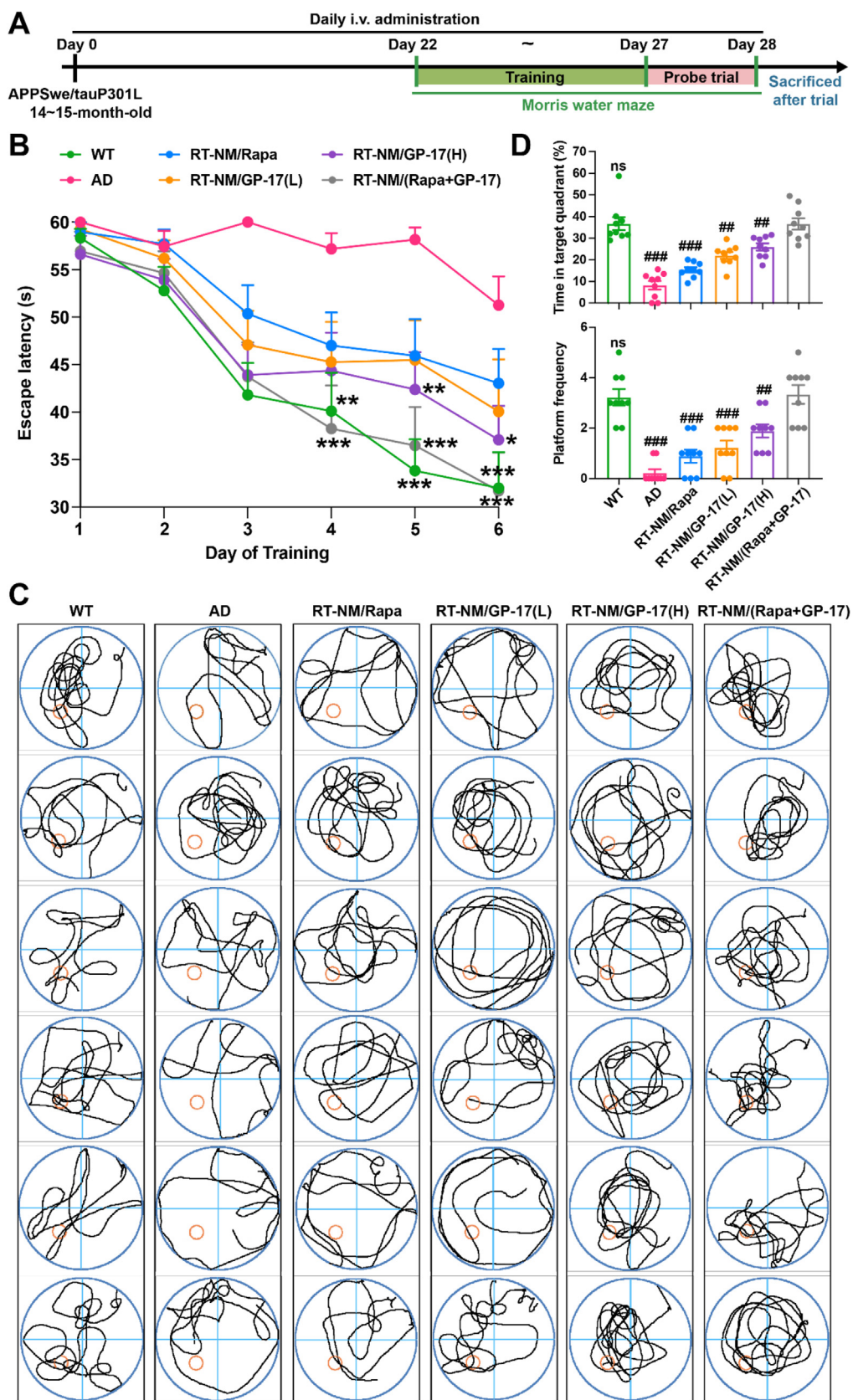


Figure 6 Rescue of spatial memory impairment in triple-transgenic mice by RT-NM/(Rapa + GP-17). (A) Timeline of the treatment and Morris water maze. $3 \times$ Tg-AD mice at 14–15 months of age were i.v. administered daily for 4 weeks, and Morris water maze experiment was conducted on the 22nd day of treatment. WT, wild-type mice dosed with saline as the normal control; AD, $3 \times$ Tg-AD mice treated with saline as the negative control; RT-NM/Rapa, 0.05 mg Rapa/kg/d; RT-NM/GP-17(L), 0.375 mg GP-17/kg/d; RT-NM/GP-17(H), 1.5 mg GP-17/kg/d;

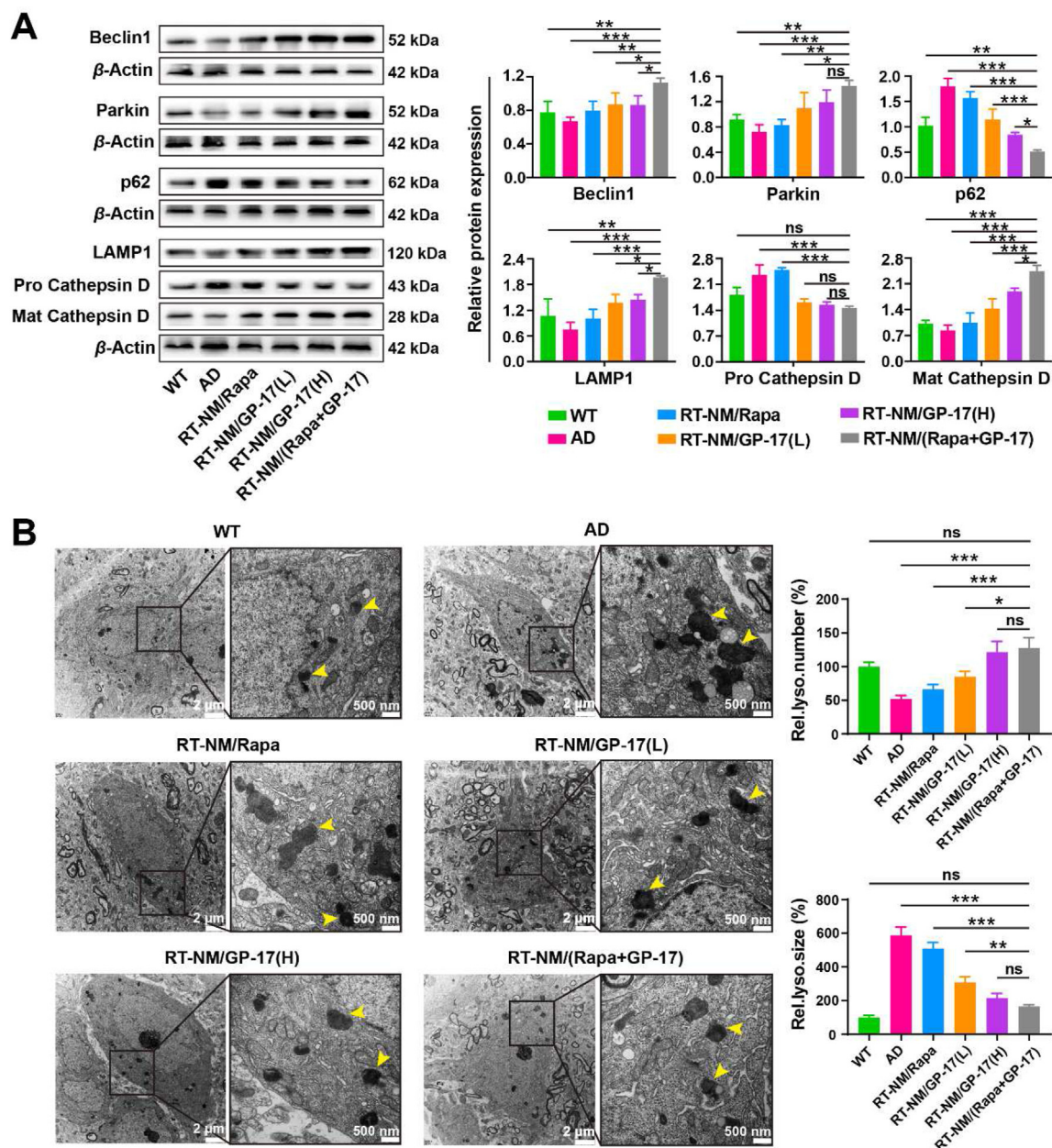


Figure 7 Restoration of autophagic flux in triple-transgenic mice by RT-NM/(Rapa + GP-17). (A) Levels of autophagic- and lysosomal-related proteins in the brains of treated 3 \times Tg-AD mice analyzed by Western blotting. Data were presented as mean \pm SD ($n = 3$). (B) Representative TEM images of lysosomes in hippocampal neurons of treated 3 \times Tg-AD mice. Yellow arrows, lysosomes. Scale bar = 2 μ m or 500 nm. Quantitative analysis of relative size and number of lysosomes by ImageJ. Data were presented as mean \pm SEM ($n = 80$ –100 lysosomes from 10 to 14 cells for size analysis and $n = 9$ –10 cells for number analysis). * $P < 0.05$, ** $P < 0.01$, *** $P < 0.001$; ns, not significant; compared with RT-NM/(Rapa + GP-17) group.

lowest $A\beta_{1-42}/A\beta_{1-40}$ ratio occurred in the RT-NM/(Rapa + GP-17) group, representing the relief of $A\beta$ pathology after RT-NM/(Rapa + GP-17) treatment. In agreement with the ELISA results, the immunohistochemical staining of $A\beta$ deposition showed that RT-NM/(Rapa + GP-17) effectively promoted the removal of

amyloid deposits with an apparent abatement in $A\beta$ loads in the hippocampus (13.4% of AD mice) and entorhinal cortex (10.7% of AD mice) (Fig. 8B and Supporting Information Fig. S10). The compromised $A\beta$ phagocytosis shown as large $A\beta$ plaques with insufficient plaque-associated microglia in AD mice was restored

RT-NM/(Rapa + GP-17), 0.05 mg Rapa/kg/d and 0.375 mg GP-17/kg/d. (B) The platform-finding latency of trained mice in spatial navigation task ($n = 9$). (C) Representative swimming traces of six trained mice of each group in probe trial test. (D) Percentage of retention time in targeted quadrant and times of platform area crossing of trained mice in probe trial test ($n = 9$). (B, D) Data were presented as mean \pm SEM. * $P < 0.05$, ** $P < 0.01$, *** $P < 0.001$, compared with AD group. # $P < 0.05$, ## $P < 0.01$, ### $P < 0.001$; ns, not significant; compared with RT-NM/(Rapa + GP-17) group.

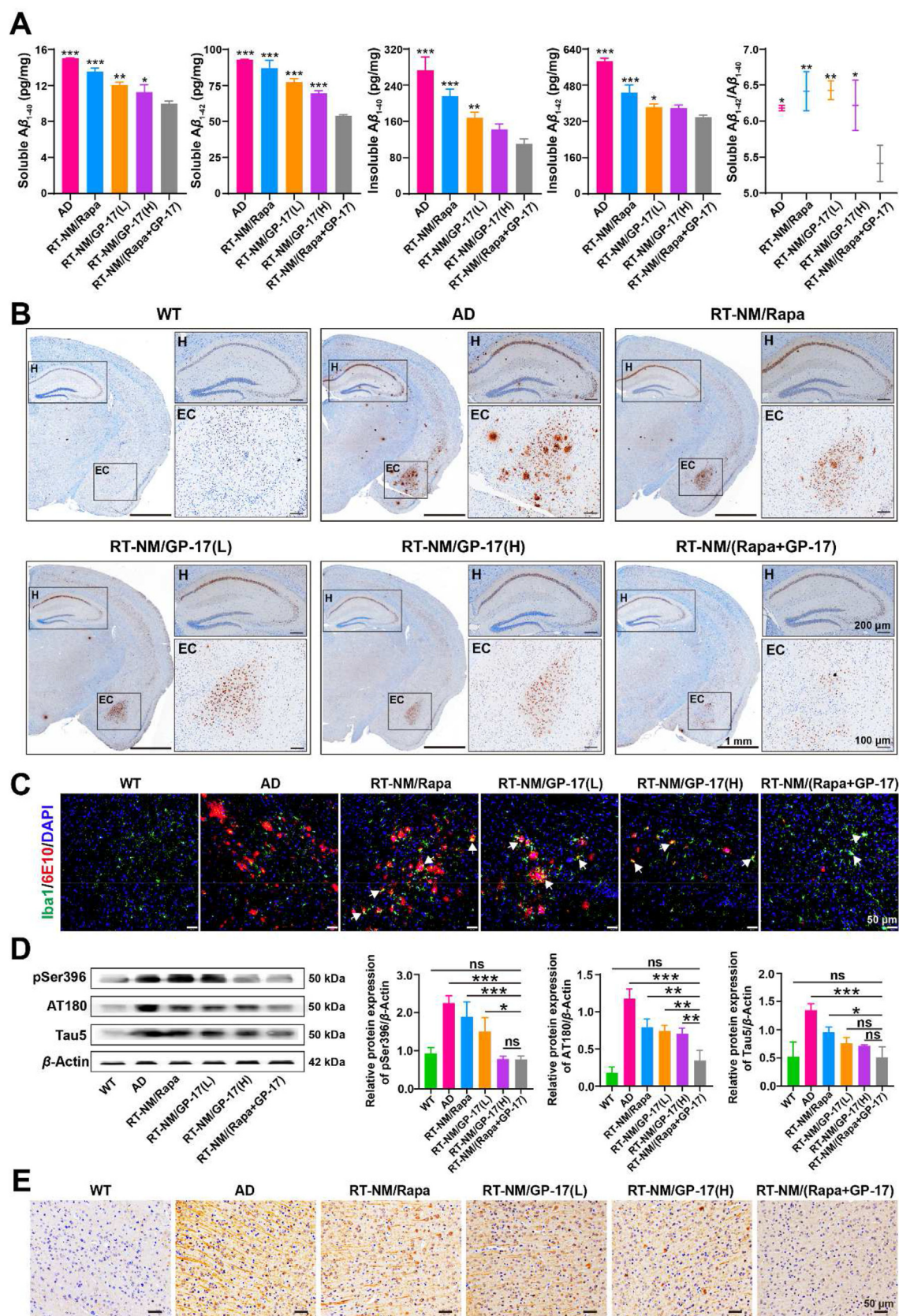


Figure 8 Reduction of $A\beta$ burden and tau hyperphosphorylation in triple-transgenic mice by RT-NM/(Rapa + GP-17). (A) Levels of soluble and insoluble $A\beta_{1-40}$ and $A\beta_{1-42}$ in the brains of treated $3 \times Tg$ -AD mice measured by ELISA ($n = 3$). (B) Representative immunohistochemical images of amyloid plaque deposit in the brains of treated $3 \times Tg$ -AD mice. The magnified insets of hippocampus (H) and entorhinal cortex (EC) were shown on the right side respectively. Scale bar = 1 mm, 200 or 100 μm . (C) Representative confocal images of cortical region in the brains

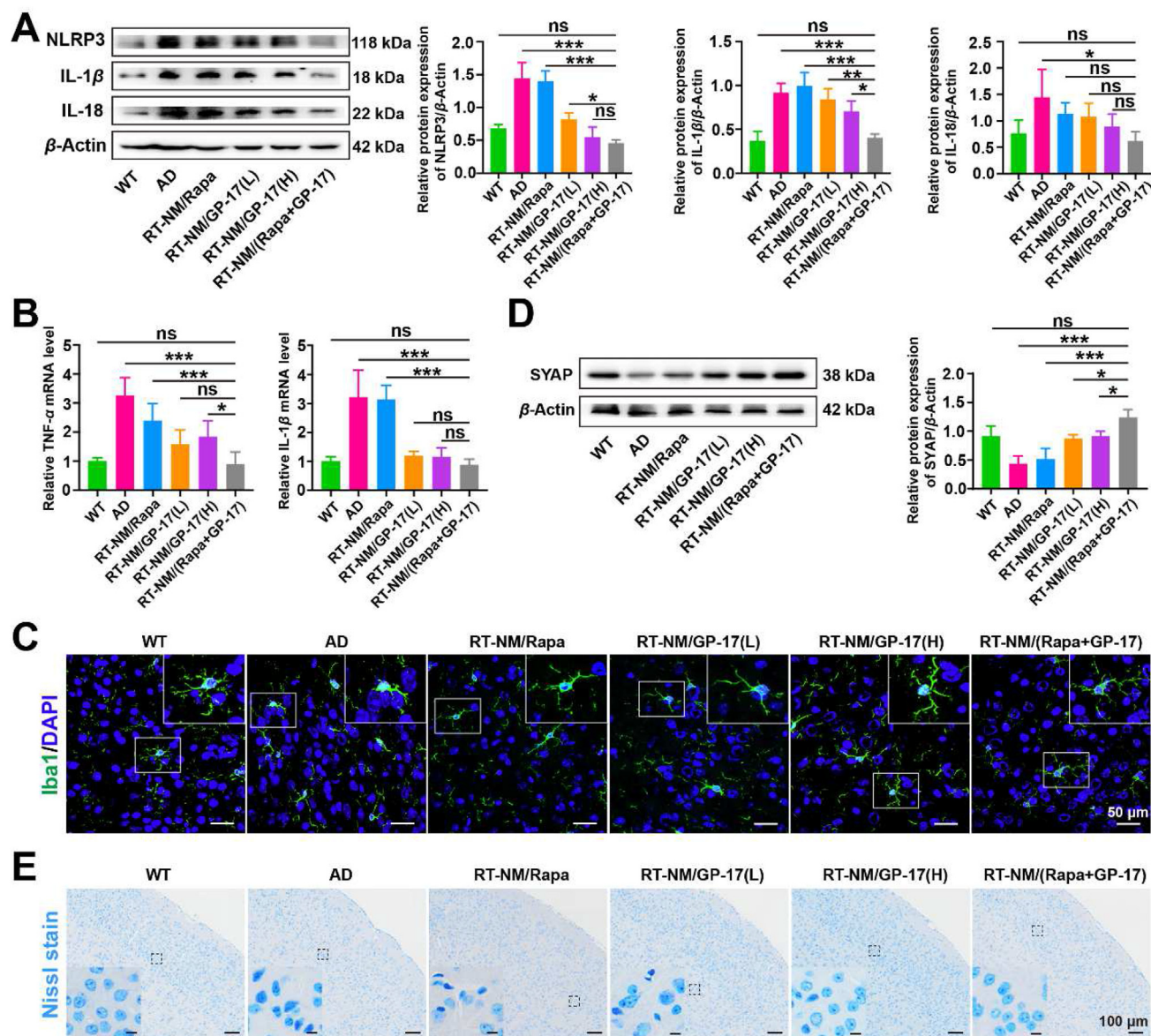


Figure 9 Neuroinflammation prevention and neuroprotection in triple-transgenic mice by RT-NM/(Rapa + GP-17). (A) Levels of inflammation-related proteins in the brains of treated 3 \times Tg-AD mice measured by Western blotting ($n = 3$). (B) Proinflammatory cytokines (TNF- α and IL-1 β) mRNA levels in the brains of treated 3 \times Tg-AD mice quantified by RT-PCR ($n = 3$). (C) Representative confocal images of cortical region in the brains of treated 3 \times Tg-AD mice. Microglia, stained with Iba1 antibody, green; Nuclei, stained with DAPI, blue. Scale bar = 50 μ m. (D) Level of synaptophysin (SYAP) in the brains of treated 3 \times Tg-AD mice analyzed by Western blotting ($n = 3$). (E) Representative Nissl staining images of cortical region in the brains of treated 3 \times Tg-AD mice. Scale bar = 100 μ m. Data were presented as mean \pm SD. * $P < 0.05$, ** $P < 0.01$, *** $P < 0.001$; ns, not significant; compared with RT-NM/(Rapa + GP-17) group.

by RT-NM/(Rapa + GP-17) treatment, as proved by smaller A β plaques with A β -colocated microglia (Fig. 8C). Predictably, the elevated p-tau level (pSer396 and AT180) and t-tau level (Tau5), and the abundant neurofibrillary tangles revealed severe tau pathology in 14–15-month-old 3 \times Tg-AD mice. Consistent with

the changes in A β pathology, tau pathology also experienced an upturn after RT-NM/(Rapa + GP-17) treatment. The levels of p-tau and t-tau descended to normal and the neurofibrillary lesions were lessened (Fig. 8D and E). The above results proved that RT-NM/(Rapa + GP-17) effectively suppressed the accumulation of

of treated 3 \times Tg-AD mice. Microglia, stained with Iba1 antibody, green; A β , stained with 6E10 antibody, red; Nuclei, stained with DAPI, blue. White arrows represent microglia colocalized with A β . Scale bar = 50 μ m. (D) Levels of p-tau (pSer396 and AT180) and t-tau (Tau5) in the brains of treated 3 \times Tg-AD mice determined by Western blotting ($n = 3$). (E) Representative immunohistochemical images of neurofibrillary tangles in the cortex of treated 3 \times Tg-AD mice brains. Scale bar = 50 μ m. Data were presented as mean \pm SD. * $P < 0.05$, ** $P < 0.01$, *** $P < 0.001$; ns, not significant; compared with RT-NM/(Rapa + GP-17) group.

A β and p-tau *in vivo*, which was largely attributable to the improved autophagic degradation.

3.9. Neuroinflammation prevention and neuroprotection in triple-transgenic mice by RT-NM/(Rapa + GP-17)

In correspondence with the *in vitro* results, the treatment of RT-NM/(Rapa + GP-17) resulted in a remarkable decrease in NLRP3 level, indicating the reduced NLRP3 inflammasome in AD mice (Fig. 9A). Since NLRP3 inflammasome serves as a platform for the maturation of interleukin-1 β (IL-1 β) and IL-18, the initiator of ensuing inflammatory cascade responses⁴⁷, the levels of IL-1 β and IL-18 were determined to evaluate NLRP3 inflammasome activity. Anticipatedly, IL-1 β and IL-18 levels lowered as the removal of NLRP3 inflammasome, proving the outstanding inhibitive effects of RT-NM/(Rapa + GP-17) on NLRP3-mediated neuroinflammation (Fig. 9A). The reduced mRNA levels of IL-1 β and tumor necrosis factor- α (TNF- α) also reflected neuroinflammation remission by RT-NM/(Rapa + GP-17) (Fig. 9B). Additionally, the alteration in microglia states was observed. The hypertrophic amoeboid microglia overwhelmingly predominated in the cortical region of AD mice, exhibiting a conversion of microglia from a resting state to a pathological overactivation state (Fig. 9C). This harmful transition was reversed to some extent by the treatment with micelles, particularly RT-NM/(Rapa + GP-17), which productively procured the retransformation of microglia into ramified shape, evincing the palliation of microglial hyperactivities. Overall, RT-NM/(Rapa + GP-17) was in favor of the remodeling of inflammatory microenvironment in AD.

Synaptic failure, precipitated by pro-inflammatory cytokines-mediated A β synaptotoxicity, is the major neurobiological basis of cognitive deficits in AD^{48–50}. As contrasted to the AD group, the significant increase in the level of synaptophysin (SYAP), a recognized marker of synaptic plasticity and function, mirrored the distinct synaptic recovery in the RT-NM/(Rapa + GP-17) group (Fig. 9D). Also, the Nissl staining analysis showed damaged neurons with shrinkage in the cortex of AD mice, while, after RT-NM/(Rapa + GP-17) treatment, noticeable neuronal recuperation with almost intact cell morphology (Fig. 9E). Together, RT-NM/(Rapa + GP-17) exhibited superior neuroprotective ability.

3.10. *In vivo* biocompatibility

Considering the long-term nature of AD treatment, it is a must to ensure the safety of administrated formulations. Therefore, the biocompatibility of RT-NM/(Rapa + GP-17) was further examined *in vivo*. After a 28-day treatment, there was no anomaly in the hematological indexes and liver and kidney function indexes of the administrated groups (Supporting Information Tables S2 and S3). And based on the H&E staining results, no obvious histopathological abnormalities occurred in major organs (Supporting Information Fig. S11). These results primarily confirmed the favorable *in vivo* biocompatibility of RT-NM/(Rapa + GP-17).

4. Discussion

Given the multitiered repercussions of autophagy, a converging pathway involved in the accepted multiplex AD pathogenesis, including amyloidosis, taupathy and neuroinflammation, on AD progression, autophagy has become an extremely appealing intervention target for AD treatment. As for autophagy regulation

strategy, what attracts attention is that emerging research has pointed out that the effectiveness or detriment of autophagy inducer as a treatment for AD is likely determined by lysosomal degradative potential⁵¹ and the autophagic cargo generation exceeding lysosomal clearance capability in turn exacerbates autophagic stress. Inspired by this, we predicted that the strategy combining autophagy induction and lysosome function improvement may attain better modulatory effects owing to the coordination of autophagosome biogenesis and degradation. For 3 \times Tg-AD mice, although there occurs lysosomal impairment at 9–10 months of age, we found that the compromised degree experiences a sharp aggravation with further aging. Therefore, this hypothesis was tested on 14–15-month-old 3 \times Tg-AD mice with severe lysosomal dysfunction which can better simulate AD, a deeply lysosomal disease^{52–54}. In concert with the reported, autophagy inducer alone had therapeutic limitations in the case of lysosomal impairment, as evidenced by the inadequate efficacy of RT-NM/Rapa (Figs. 6–9). Intriguingly, RT-NM/GP-17 at high dosage (1.5 mg/kg/d) generated rather positive effects, reflecting the outstanding role of lysosomal defects remediation in autophagy regulation (Fig. 7). Supporting our conjecture, co-therapeutic micelles (RT-NM/(Rapa + GP-17)) demonstrated therapeutic superiority over monotherapeutic micelles (RT-NM/Rapa or RT-NM/GP-17), even at low GP-17 dosage (0.375 mg/kg/d), underscoring that this combination regulation strategy could heighten efficacy with a reduced dose, which is beneficial for safety control of autophagy intervention. The co-elevation of autophagic level and lysosomal degradative potential contributed to the autophagy state transition from stasis to patency, which then resulted in the increased clearance of autophagy substrates, such as A β , p-tau and inflammasome. These results verified the reasonableness of the regulatory conception changeover from simple autophagy induction to autophagic homeostasis rehabilitation, especially for diseases, like AD, in the context of which autophagy impairment is a multistage dysregulation. Under its guidance, there are chances of developing more effective avenues with enhanced fit with pathological conditions for autophagy regulation.

The appropriate choice of target cell is indispensable for therapeutic success. Since neurons are post-mitotic, long-lived cells with high susceptibleness to neurotoxicity and immensely depend on autophagy to realize robust protein and organelle quality control, scores of autophagy-targeted therapies strive to improve neuronal autophagic function. For instance, Sun et al.⁵⁵ developed a nanoassembly to activate neuronal autophagy for detoxification of pathogenic tau, rescuing neuron viability and alleviating the cognitive impairment in AD. As more in-depth investigations into autophagy impairment in AD, the unveiled important role of microglial autophagy in AD pathological process has gradually drawn more research attention to therapies aiming at defective microglia autophagy. Yang et al.⁵⁶ reported a multipronged nanoparticle to induce microglia autophagy activation for removal of A β and tau deposition and reshaping of inflammatory microenvironment, thereby relieving the AD symptoms. Although these autophagy-targeted therapies acting on single-type cells perform well in AD treatment, considering the intricate pathological interaction of neurons and microglia with autophagy as a pivotal common node, simultaneous regulation of neuronal and microglia autophagy is theoretically hopeful to gain therapeutic outperformance. Based on this speculation, a benign therapeutic network was constructed in our study. The improved neuronal autophagy significantly decreased the intraneuronal accumulation of A β and p-tau, thereby

remitting loss of proteostasis in neurons. Meanwhile, extra-neuronal A β deposition, the trigger of microglia overactivation and further detrimental neuroinflammation, was effectively eliminated by microglia phagocytosis which was restored *via* microglia autophagy melioration. Besides the removal of A β , the potentiated autophagic clearance of NLRP3 inflammasome in microglia also abated neuroinflammation. Eventually, the damaged neurons experienced a prominent recovery benefiting from the holistic protection formed by the co-betterment of intraneuronal proteostasis and extraneuronal inflammatory microenvironment.

Effective drug delivery to both neurons and microglia at AD lesion sites is a requisite for the implementation of the above-proposed autophagy-targeted therapeutic strategy. Receptor/ligand binding-based active targeting is the most applied targeting approach whose efficiency hinges to a large extent on the receptor expression pattern and the ligand-to-receptor affinity. RAGE, belonging to the immunoglobulin superfamily of cell surface molecules⁵⁷, is a cellular binding site for A β and mediates its uptake and transport from blood into brain. As a receptor implicated in AD progression, the expression of RAGE is markedly elevated in BBB, neurons, and microglia in the AD-affected region and appears positive correlation with the severity of AD pathology^{58,59}. Founded on its AD-evoked expression change, RAGE was an ideal targeting receptor. Correspondingly, RP-1, a peptide with high homology to the 16–23 (KLVFFAED) region in A β peptide, the major A β -RAGE binding site⁶⁰, was chosen as targeting ligand by virtue of its high affinity to RAGE and non-toxicity. As expected, RP-1-modified micelles showed enhanced BBB penetration, specific distribution in diseased regions, and further enrichment in neurons and microglia with gratifying targeting specificity. Of note, this cascade dual-targeting was realized by single ligand modification, suggesting that our study provided a concise design for lesion-specific neuron-and-microglia co-targeting delivery system.

Altogether, we have designed a comprehensive scheme, embracing the optimized regulatory strategy improving entire autophagy-lysosome pathway, the careful target cell selection building multi-dimensional neuroprotection system, and the proper targeting design accomplishing specific delivery, so as to render therapeutic effects of autophagy-targeted therapy to the utmost for AD treatment. The ultimate cognition restoration of 3 \times Tg-AD transgenic mice by the accordingly-constructed RT-NM/(Rapa + GP-17) demonstrated the immense potential of AD therapy formulated herein.

Notwithstanding, our study is just a preliminary exploration on the therapeutic potential of multidimensional autophagy regulation for AD, and is not enough to support its clinical application. There are still several key points left for further investigation. First, the systematic screening of drug dosages *in vivo*, an indispensable part in optimizing the scheme of combination therapy, is needed to be performed in follow-up research. Second, as autophagy state varies at different stages of AD, the temporal window to modulate autophagy is of importance for efficacy. Thus, the screening of intervention time point should be included in future studies.

5. Conclusions

In summary, we developed a pathologically-oriented autophagy-targeted therapy for AD treatment, which focused on the two key links of the autophagy-lysosome pathway, autophagy activation and lysosomal degradation, and withal took both neurons and microglia as regulatory targeting cells. A nano-combination

system, RT-NM/(Rapa + GP-17) was established to achieve the precise delivery of drugs to targeted cells, neurons and microglia in AD lesions, and the following efficient ROS-responsive drug release. RT-NM/(Rapa + GP-17) possessed distinguished regulative effects on the entire autophagy-lysosome pathway, thereby ensuring autophagy flux patency for clearance of pathologically accumulated protein aggregates, including A β , p-tau and inflammasome. Based on this, RT-NM/(Rapa + GP-17) effectively restored neuron homeostasis and alleviated neuroinflammation, finally ameliorating cognitive defects in 3 \times Tg-AD transgenic mice. Our attempt at combined modulation on the different stages of autophagy-lysosome pathway in pathological-interactive cells is of reference significance for autophagy-targeted therapy development and is promising to be expanded to the treatment of other neurodegenerative diseases.

Acknowledgments

This study was supported by National Natural Science Foundation of China (Nos. 82073780 and 82273868, China), and Shanghai Municipal Natural Science Foundation (No. 19ZR1406200, China). The author would like to thank the staff members of the Integrated Laser Microscopy System at the National Facility for Protein Science in Shanghai (NFPS), Shanghai Advanced Research Institute, Chinese Academy of Sciences, China for sample preparation, data collection and analysis.

Author contributions

Qizhi Zhang, Yixian Li, Peng Yang and Ran Meng designed the research. Yixian Li, Peng Yang and Ran Meng carried out the experiments and performed data analysis. Lingling Zhou, Kang Qian, Yunlong Cheng, Dongyu Sheng and Tianying Wang participated part of the experiments. Shuting Xu, Pengzhen Wang, Minjun Xu, Jing Wu and Jinxu Cao provided experimental drugs and quality control. Yixian Li wrote the manuscript. Qizhi Zhang, Ran Meng and Peng Yang revised the manuscript. All of the authors have read and approved the final manuscript.

Conflicts of interest

The authors have no conflicts of interest to declare.

Appendix A. Supporting information

Supporting data to this article can be found online at <https://doi.org/10.1016/j.apsb.2023.10.009>.

References

1. Park H, Kang JH, Lee S. Autophagy in neurodegenerative diseases: a hunter for aggregates. *Int J Mol Sci* 2020;**21**:3369.
2. Bloom GS. Amyloid- β and tau: the trigger and bullet in Alzheimer disease pathogenesis. *JAMA Neurol* 2014;**71**:505–8.
3. Cai Q, Ganesan D. Regulation of neuronal autophagy and the implications in neurodegenerative diseases. *Neurobiol Dis* 2022;**162**:105582.
4. Di Meo A, Curtis ME, Lauretti E, Praticò D. Autophagy dysfunction in Alzheimer's disease: mechanistic insights and new therapeutic opportunities. *Biol Psychiatr* 2020;**87**:797–807.
5. Heckmann BL, Teubner BJW, Tummers B, Boada-Romero E, Harris L, Yang M, et al. LC3-associated endocytosis facilitates β -

- amyloid clearance and mitigates neurodegeneration in murine Alzheimer's disease. *Cell* 2019;**178**:536–51.e14.
6. Plaza-Zabala A, Sierra-Torre V, Sierra A. Autophagy and microglia: novel partners in neurodegeneration and aging. *Int J Mol Sci* 2017;**18**:598.
 7. Cho MH, Cho K, Kang HJ, Jeon EY, Kim HS, Kwon HJ, et al. Autophagy in microglia degrades extracellular β -amyloid fibrils and regulates the NLRP3 inflammasome. *Autophagy* 2014;**10**:1761–75.
 8. Wu AG, Zhou XG, Qiao G, Yu L, Tang Y, Yan L, et al. Targeting microglial autophagic degradation in NLRP3 inflammasome-mediated neurodegenerative diseases. *Ageing Res Rev* 2021;**65**:101202.
 9. Kim KH, Lee MS. Autophagy—a key player in cellular and body metabolism. *Nat Rev Endocrinol* 2014;**10**:322–37.
 10. Menzies FM, Fleming A, Caricasole A, Bento CF, Andrews SP, Ashkenazi A, et al. Autophagy and neurodegeneration: pathogenic mechanisms and therapeutic opportunities. *Neuron* 2017;**93**:1015–34.
 11. Bové J, Martínez-Vicente M, Vila M. Fighting neurodegeneration with rapamycin: mechanistic insights. *Nat Rev Neurosci* 2011;**12**:437–52.
 12. Ozcelik S, Fraser G, Castets P, Schaeffer V, Skachokova Z, Breu K, et al. Rapamycin attenuates the progression of tau pathology in P301S tau transgenic mice. *PLoS One* 2013;**8**:e62459.
 13. Meng XB, Luo Y, Liang T, Wang MX, Zhao JY, Sun GB, et al. Gypenoside XVII enhances lysosome biogenesis and autophagy flux and accelerates autophagic clearance of amyloid- β through TFEB activation. *J Alzheimers Dis* 2016;**52**:1135–50.
 14. Tramutola A, Lanzillotta C, Di Domenico F. Targeting mTOR to reduce Alzheimer-related cognitive decline: from current hits to future therapies. *Expert Rev Neurother* 2017;**17**:33–45.
 15. Galluzzi L, Bravo-San Pedro JM, Levine B, Green DR, Kroemer G. Pharmacological modulation of autophagy: therapeutic potential and persisting obstacles. *Nat Rev Drug Discov* 2017;**16**:487–511.
 16. Mao JZ, Wang H, Xie Y, Fu YX, Li YC, Liu P, et al. Transdermal delivery of rapamycin with poor water-solubility by dissolving polymeric microneedles for anti-angiogenesis. *J Mater Chem B* 2020;**8**:928–34.
 17. Brandt C, Hillmann P, Noack A, Römermann K, Öhler LA, Rageot D, et al. The novel, catalytic mTORC1/2 inhibitor PQR620 and the PI3K/mTORC1/2 inhibitor PQR530 effectively cross the blood-brain barrier and increase seizure threshold in a mouse model of chronic epilepsy. *Neuropharmacology* 2018;**140**:107–20.
 18. Zhao F, Zhao Y, Liu Y, Chang XL, Chen CY, Zhao YL. Cellular uptake, intracellular trafficking, and cytotoxicity of nanomaterials. *Small* 2011;**7**:1322–37.
 19. Fröhlich E. Cellular elimination of nanoparticles. *Environ Toxicol Pharmacol* 2016;**46**:90–4.
 20. He XQ, Wang XR, Yang LY, Yang ZH, Yu WQ, Wang YZ, et al. Intelligent lesion blood-brain barrier targeting nano-missiles for Alzheimer's disease treatment by anti-neuroinflammation and neuroprotection. *Acta Pharm Sin B* 2022;**12**:1987–99.
 21. Lei T, Yang ZH, Xia X, Chen YX, Yang XT, Xie R, et al. A nanocleaner specifically penetrates the blood-brain barrier at lesions to clean toxic proteins and regulate inflammation in Alzheimer's disease. *Acta Pharm Sin B* 2021;**11**:4032–44.
 22. Xu ST, Yang P, Qian K, Li YX, Guo Q, Wang PZ, et al. Modulating autophagic flux via ROS-responsive targeted micelles to restore neuronal proteostasis in Alzheimer's disease. *Bioact Mater* 2021;**11**:300–16.
 23. Lue LF, Walker DG, Brachova L, Beach TG, Rogers J, Schmidt AM, et al. Involvement of microglial receptor for advanced glycation endproducts (RAGE) in Alzheimer's disease: identification of a cellular activation mechanism. *Exp Neurol* 2001;**171**:29–45.
 24. Kong YY, Liu CP, Zhou YP, Qi JX, Zhang CC, Sun BM, et al. Progress of RAGE molecular imaging in Alzheimer's disease. *Front Aging Neurosci* 2020;**12**:227.
 25. Zlokovic BV. New therapeutic targets in the neurovascular pathway in Alzheimer's disease. *Neurotherapeutics* 2008;**5**:409–14.
 26. Cai CZ, Dai XY, Zhu YJ, Lian MY, Xiao F, Dong FY, et al. A specific RAGE-binding peptide biopanning from phage display random peptide library that ameliorates symptoms in amyloid β peptide-mediated neuronal disorder. *Appl Microbiol Biotechnol* 2016;**100**:825–35.
 27. Kimbrough IF, Robel S, Roberson ED, Sontheimer H. Vascular amyloidosis impairs the gliovascular unit in a mouse model of Alzheimer's disease. *Brain* 2015;**138**:3716–33.
 28. Guo Q, Xu ST, Yang P, Wang PZ, Lu S, Sheng DY, et al. A dual-ligand fusion peptide improves the brain-neuron targeting of nanocarriers in Alzheimer's disease mice. *J Control Release* 2020;**320**:347–62.
 29. Lee JH, Yu WH, Kumar A, Lee S, Mohan PS, Peterhoff CM, et al. Lysosomal proteolysis and autophagy require presenilin 1 and are disrupted by Alzheimer-related PS1 mutations. *Cell* 2010;**141**:1146–58.
 30. Guo Q, Li YX, Xu ST, Wang PZ, Qian K, Yang P, et al. Brain-neuron targeted nanoparticles for peptide synergy therapy at dual-target of Alzheimer's disease. *J Control Release* 2023;**355**:604–21.
 31. Hu BB, Dai FY, Fan ZM, Ma GH, Tang QW, Zhang X. Nanotheranostics: Congo red/rutin-MNPs with enhanced magnetic resonance imaging and H₂O₂-responsive therapy of Alzheimer's disease in APP^{swE}/PS1^{dE9} transgenic mice. *Adv Mater* 2015;**27**:5499–505.
 32. Xia HM, Gao XL, Gu GZ, Liu ZY, Hu QY, Tu YF, et al. Penetratin-functionalized PEG-PLA nanoparticles for brain drug delivery. *Int J Pharm* 2012;**436**:840–50.
 33. Gao XL, Tao WX, Lu W, Zhang QZ, Zhang Y, Jiang XG, et al. Lectin-conjugated PEG-PLA nanoparticles: preparation and brain delivery after intranasal administration. *Biomaterials* 2006;**27**:3482–90.
 34. Fu HJ, Hardy J, Duff KE. Selective vulnerability in neurodegenerative diseases. *Nat Neurosci* 2018;**21**:1350–8.
 35. Lee S, Sato Y, Nixon RA. Primary lysosomal dysfunction causes cargo-specific deficits of axonal transport leading to Alzheimer-like neuritic dystrophy. *Autophagy* 2011;**7**:1562–3.
 36. Aits S, Krickler J, Liu B, Ellegaard AM, Hämälistö S, Tvingsholm S, et al. Sensitive detection of lysosomal membrane permeabilization by lysosomal galectin puncta assay. *Autophagy* 2015;**11**:1408–24.
 37. Martini-Stoica H, Xu Y, Ballabio A, Zheng H. The Autophagy-lysosomal pathway in neurodegeneration: a TFEB perspective. *Trends Neurosci* 2016;**39**:221–34.
 38. Jaeger PA, Wyss-Coray T. Beclin 1 complex in autophagy and Alzheimer disease. *Arch Neurol* 2010;**67**:1181–4.
 39. Lee JW, Nam H, Kim LE, Jeon Y, Min H, Ha S, et al. TLR4 (toll-like receptor 4) activation suppresses autophagy through inhibition of FOXO₃ and impairs phagocytic capacity of microglia. *Autophagy* 2019;**15**:753–70.
 40. Bonilla DL, Bhattacharya A, Sha YB, Xu Y, Xiang Q, Kan A, et al. Autophagy regulates phagocytosis by modulating the expression of scavenger receptors. *Immunity* 2013;**39**:537–47.
 41. Ma C, Hong FF, Yang SL. Amyloidosis in Alzheimer's disease: pathogeny, etiology, and related therapeutic directions. *Molecules* 2022;**27**:1210.
 42. Congdon EE, Wu JW, Myeku N, Figueroa YH, Herman M, Marinec PS, et al. Methylthionium chloride (methylene blue) induces autophagy and attenuates tauopathy *in vitro* and *in vivo*. *Autophagy* 2012;**8**:609–22.
 43. Liu Y, Dai Y, Li Q, Chen C, Chen H, Song YJ, et al. Beta-amyloid activates NLRP3 inflammasome via TLR4 in mouse microglia. *Neurosci Lett* 2020;**736**:135279.
 44. Jiang SY, Maphis NM, Binder J, Chisholm D, Weston L, Duran W, et al. Proteopathic tau primes and activates interleukin- β via myeloid-cell-specific MyD88- and NLRP3-ASC-inflammasome pathway. *Cell Rep* 2021;**36**:109720.
 45. Drummond E, Wisniewski T. Alzheimer's disease: experimental models and reality. *Acta Neuropathol* 2017;**133**:155–75.
 46. Kwak SS, Washicosky KJ, Brand E, von Maydell D, Aronson J, Kim S, et al. Amyloid- β 42/40 ratio drives tau pathology in 3D human neural cell culture models of Alzheimer's disease. *Nat Commun* 2020;**11**:1377.
 47. Jha D, Bakker ENTP, Kumar R. Mechanistic and therapeutic role of NLRP3 inflammasome in the pathogenesis of Alzheimer's disease. *J Neurochem* 2023. Available from: <https://onlinelibrary.wiley.com/doi/10.1111/jnc.15788>.

48. Marttinen M, Takalo M, Natunen T, Wittrahm R, Gabbouj S, Kempainen S, et al. Molecular mechanisms of synaptotoxicity and neuroinflammation in Alzheimer's Disease. *Front Neurosci* 2018;**12**:963.
49. Mitew S, Kirkcaldie MTK, Dickson TC, Vickers JC. Altered synapses and gliotransmission in Alzheimer's disease and AD model mice. *Neurobiol Aging* 2013;**34**:2341–51.
50. Rizzo FR, Musella A, De Vito F, Fresegna D, Bullitta S, Vanni V, et al. Tumor necrosis factor and interleukin-1 β modulate synaptic plasticity during neuroinflammation. *Neural Plast* 2018;**2018**:8430123.
51. Carosi JM, Sargeant TJ. Rapamycin and Alzheimer disease: a hypothesis for the effective use of rapamycin for treatment of neurodegenerative disease. *Autophagy* 2023;**19**:2386–90.
52. Lai SSM, Ng KY, Koh RY, Chok KC, Chye SM. Endosomal-lysosomal dysfunctions in Alzheimer's disease: pathogenesis and therapeutic interventions. *Metab Brain Dis* 2021;**36**:1087–100.
53. Gao S, Casey AE, Sargeant TJ, Mäkinen VP. Genetic variation within endolysosomal system is associated with late-onset Alzheimer's disease. *Brain* 2018;**141**:2711–20.
54. Lee JH, Yang DS, Goulbourne CN, Im E, Stavrides P, Pensalfini A, et al. Faulty autolysosome acidification in Alzheimer's disease mouse models induces autophagic build-up of A β in neurons, yielding senile plaques. *Nat Neurosci* 2022;**25**:688–701.
55. Sun H, Zhong Y, Zhu XD, Liao HW, Lee JY, Chen Y, et al. A Tauopathy-homing and autophagy-activating nanoassembly for specific clearance of pathogenic tau in Alzheimer's disease. *ACS Nano* 2021;**15**:5263–75.
56. Yang XT, Yang WQ, Xia X, Lei T, Yang ZH, Jia WF, et al. Intranasal delivery of BACE1 siRNA and rapamycin by dual targets modified nanoparticles for Alzheimer's disease therapy. *Small* 2022;**18**:e2203182.
57. Xue J, Rai V, Singer D, Chabierski S, Xie JJ, Reverdatto S, et al. Advanced glycation end product recognition by the receptor for AGEs. *Structure* 2011;**19**:722–32.
58. Yan SD, Chen X, Fu J, Chen M, Zhu H, Roher A, et al. RAGE and amyloid-beta peptide neurotoxicity in Alzheimer's disease. *Nature* 1996;**382**:685–91.
59. Zlokovic BV. Neurovascular pathways to neurodegeneration in Alzheimer's disease and other disorders. *Nat Rev Neurosci* 2011;**12**:723–38.
60. Jargito A, Grabowska I, Radecka H, Sulima M, Marszałek I, Wysłouch-Cieszyńska A, et al. Redox active dipyrromethene-Cu(II) monolayer for oriented immobilization of His-tagged RAGE domains—the base of electrochemical biosensor for determination of A β_{16-23} . *Electroanalysis* 2013;**25**:1185–93.